On the choice and implications of rheologies that maintain kinematic and dynamic consistency over the entire earthquake cycle

Rishav Mallick[1,2], Valère Lambert[3], and Brendan Meade[4]

[1]Seismological Laboratory, California Institute of Technology
[2]Earth Observatory of Singapore, Nanyang Technological University, Singapore
[3]Seismological Laboratory, University of California, Santa Cruz
[4]Department of Earth and Planetary Sciences, Harvard University

April 28, 2022

Abstract

Viscoelastic processes in the upper mantle redistribute seismically generated stresses and modulate crustal deformation rates throughout the earthquake cycle. Geodetic observations of these motions at the surface of the coupled crust-mantle system offer the possibility of constraining the rheology of the upper mantle and the rates of stress transfer during the intervals between large earthquakes. Parsimonious representations of viscoelastically modulated deformation through the aseismic phase of the earthquake cycle should be able to simultaneously explain decadal-scale geodetic observations of both rapid postseismic deformation and late in the earthquake cycle near-fault strain localization. To understand how a choice of rheological formulation affects kinematics, we compare predictions from time-dependent forward models of deformation over the entire earthquake cycle on and surrounding an idealized vertical strike-slip fault in a homogeneous elastic crust underlain by a homogeneous viscoelastic upper mantle. We explore three different rheologies as inferred from laboratory experiments: 1) linear Maxwell, 2) linear Burgers, and 3) power-law. Both the linear Burgers and power-law rheological models can be made consistent with fast and slow deformation phenomenology from across the entire earthquake cycle, while the single-layer linear Maxwell model cannot. The kinematic similarity of both linear Burgers and power-law rheology models suggests that geodetic observations alone may be insufficient to distinguish between these two rheologies, but do indicate that one may serve as an effective proxy for the other. Additionally, the power-law rheology model displays a postseismic response that is strongly earthquake magnitude dependent, which may offer a partial explanation for observations of limited postseismic deformation near some magnitude 6.5-7.0 earthquakes. We discuss the role of mechanical coupling between frictional slip and viscous creep in controlling the time-dependence of regional stress transfer following large earthquakes and how this may affect the seismic hazard and risk to communities living close to fault networks.

Plain Language Summary

The solid Earth is a viscoelastic material that displays both solid and fluid-like behaviors depending on the observational time window and the applied stress. We develop numerical simulations of how the uppermost solid Earth responds to a sequence of periodic earthquakes and the earthquake cycle. Our simulations test a range of proposed viscoelastic materials. The predicted surface displacements from each model are compared with observational features extracted from geodetic datasets compiled over the past few decades. All existing viscoelastic material descriptions can satisfactorily explain observational features in the first few years following an earthquake; significant differences between the viscoelastic models emerge 10 - 100 years following a large earthquake. Identifying the most appropriate viscoelastic description requires the integration of geodetic data that constrains the velocity evolution from a sequence of earthquakes (as opposed to a single event) with observations from rock physics laboratory experiments. A unified description of visceolasticity in the upper most solid earth has important implications for understanding stress evolution in fault networks, and improving models of seismic hazard.

1 Introduction

Inferring the constitutive relations that describe how the macroscopic stress state of the lithosphere-asthenosphere system evolves as a function of strain rate, total strain and intensive system variables (temperature, pressure, composition, etc.) remains a grand challenge in the geosciences [NSF, 2020]. Constraining these constitutive relations, or rheology, is fundamental to our understanding of the dynamics of the solid Earth. From the occurrence of earthquakes and their effects at any point within the Earth, to the construction of the geological structure that surrounds us and the sustenance of plate tectonics itself, the rheology and strength of Earth materials plays a crucial role in defining these processes [*Bürgmann and Dresen*, 2008; *Mulyukova and Bercovici*, 2019]. However, inferring these constitutive relations at the length scale of geological processes (>1 kilometer) is a difficult task as aspects of rock failure are shown to be scale-dependent [e.g., *Yamashita et al.*, 2015; *Lambert et al.*, 2021] and there are limited opportunities to conduct experiments at the crustal or lithospheric scale. Our goal in this article is to demonstrate that the earthquake cycle, in the vicinity of a mature strike-slip fault, may provide us with the necessary experimental conditions to probe the rheology of the lithosphere.

While there exist a number of studies that have sought to infer rheological properties of Earth's lithosphere-asthenosphere system using observations from the earthquake cycle [*Bürgmann and Dresen*, 2008, and references therein], the interpretation of results from different methodologies for extracting rheological parameters can be limited or challenged by three key assumptions. First, a common approach to modeling geophysical systems is to prescribe a functional form of the rheological model a priori and then estimate the associated best-fitting set of rheological parameters for that selected model, potentially with limited consideration of alternative rheological models that may be equally or better supported by the observations. Second, studies are often limited to a specific observational time window, such as a few years following an earthquake, from which the aforementioned best-fit model parameters are estimated. As such, inferred parameters are tied to the observational window that is probed, which may in part explain vastly different rheological estimates determined for studies of the lithosphere over different observational windows [e.g., *Pollitz*, 2005, 2019; *Ryder et al.*, 2007; *Henriquet et al.*, 2019; *Tamisiea et al.*, 2007; *Milne et al.*, 2001; *Hussain et al.*, 2018; *Larsen et al.*, 2005; *Kaufmann and Amelung*, 2000]. Finally, a common assumption when processing observed time series is that the signal can be well-separated into a set of

linearly superimposed functions, thereby neglecting nonlinear interactions among the associated physical processes.

In this work, we seek to develop a framework that overcomes some of these limitations and can reconcile rheological inferences from different observational windows. As a starting point, we focus on major observational features in geodetic time series obtained from mature strike-slip fault settings globally, from immediately following earthquakes (postseismic period) to late in the earthquake cycle (interseismic period). We do not attempt to directly optimize the fit to data, rather we consider the generality and descriptive power of popular rheological models of the lithosphere and study where each model can explain major observational features or is insufficient [*Tarantola*, 2006]. To assist the reader with appreciating the task at hand, we begin by providing some background on common rheological models that are used to describe lithospheric deformation, general observational constraints available from geodesy and prevalent modeling strategies in the literature.

1.1 Elasticity, friction and viscous creep

The rheology of the lithosphere does not appear to follow a single simple description at all timescales. For example, the passage of seismic waves and the static displacement or deformation of Earth's lithosphere in response to an earthquake tell us that the lithosphere can be described as an elastic body over timescales ranging from seconds to a day. However, the entire lithosphere cannot be elastic since the earthquake source itself is an inelastic process, generally considered to be a frictional rupture restricted to a narrow shear band [*Kanamori and Brodsky*, 2004].

At timescales longer than a day, time-dependent deformation patterns of the solid Earth's surface following large earthquakes is routinely imaged using geodetic and remote sensing observational techniques [*Avouac*, 2015]. These datasets reveal the non-elastic nature of the lithosphere i.e., deformation that continues well after the initial source of deformation has ceased.

This observed time-dependent post-seismic deformation is thought to result from a combination of two different processes: (1) time-dependent frictional slip on fault planes (afterslip) while the surrounding medium is elastic, and (2) time-dependent deformation of the entire medium itself. Afterslip is thought to be limited to depths where frictional processes are mechanically favourable and is typically modelled as $\sigma \propto \log(\dot{\varepsilon})$, where $\dot{\varepsilon}$ is the strain rate, σ is stress in the body [*Marone et al.*, 1991]. Beyond this domain, distributed deformation of rocks in the form of Newtonian and power-law processes are thought to dominate deformation styles [*Montési*, 2004; *Hirth and Kohlstedt*, 2003]. Distributed deformation of the medium is commonly thought to be a viscoelastic process where the short timescale stress perturbations are accommodated by the elasticity of the medium ($\varepsilon \propto \sigma$) while relaxation following instantaneous stress steps or long timescale observations highlight the viscous properties of the medium i.e., $\dot{\varepsilon} \propto \sigma^n$ (ε - strain, $\dot{\varepsilon}$ - strain rate, n - power exponent, σ - stress) [*Karato et al.*, 1986]. Laboratory experiments also suggest that viscous flow laws exhibit unsteady or transient deformation i.e., the relationship between σ and $\dot{\varepsilon}$ is unique once steady state is achieved, which requires a finite amount of strain or time [*Post*, 1977]. This style of deformation is often modeled using a Burgers rheology [e.g., *Müller*, 1986; *Hetland and Hager*, 2005].

1.2 Geodetic observations

Over the last three decades, space-based geodetic observations have provided direct observations of deformation throughout the earthquake cycle. As a result, tectonic processes associated with

the preseismic and postseismic timescales are well imaged, and we derive and discuss only the major features from these observations. In this study, we focus on mature strike-slip faults and simplify them to a two-dimensional geometry and describe the characteristics of the interseismic and postseismic period as imaged by geodetic techniques - the interseismic locking depth, the postseismic relaxation time and cumulative postseismic deformation over a given time window. These are key features that numerical models of the earthquake cycles along such faults attempt to explain.

1.2.1 Interseismic observations

In between earthquakes, geodetic time series from most mature strike-slip fault settings appear nearly linear in time, at least over available observational timescales (1-2 decades), and the estimated velocities follow an S-shaped function in space, commonly modeled using the $\tan^{-1}$ operator (Figure 1) [e.g., *Vernant*, 2015; *Savage and Burford*, 1973]. Deviations from this expected behavior do appear in the data, such as non-linearities in the time series and deviations from the $\tan^{-1}$ shape function , however these differences are mostly due to localized creep episodes (in time and space) or time-invariant creep on some sections of the fault.

Geodetic velocities are typically fit well with the functional form $\frac{v^{\infty}}{\pi}\tan^{-1}\left(\frac{x}{x_d}\right)$, where v^{∞} is the estimated long-term slip rate on the fault and D_{lock} is the depth to which the fault is locked; beyond this depth, the entire fault is assumed to creep along an infinitesimally narrow shear surface at a time-invariant rate of v^{∞}. Studies show that v^{∞} estimates for major strike-faults globally match the estimated geological slip rates of the same faults within measurement uncertainties [*Meade et al.*, 2013]. The estimated locking depth from this kind of modeling is on the order of $10-20$ km, which is comparable to the thickness of the lithosphere over which frictional processes are thought to be dominant [*Vernant*, 2015].

1.2.2 Postseismic observations

Following large earthquakes, time-dependent deformation occurs in the near-field as well as far away from the fault. This time-dependent signal is typically decomposed into a linear term and a decaying curvature term, i.e., a monotonic function that is bounded between 0 and its maximum value (Figure 1). The linear term is assumed to represent background loading due to the motion of tectonic plates. The curvature in the timeseries is typically fit with functional forms such as $\log(t/t_R+1)$ and e^{-t/t_R}, motivated by spring-slider models of afterslip and creep of a linear viscoelastic material respectively [*Perfettini and Avouac*, 2004]. t_R in each case refers to a relaxation time of the corresponding physical process. Poroelastic deformation can also contribute to postseismic deformation [*Peltzer et al.*, 1998; *Jónsson et al.*, 2003], however we ignore this process as we are limited to a two-dimensional anti-plane geometry where no volumetric strains occur.

Deformation due to fault afterslip is expected to be dominant at observation sites close to the fault, and can be reasonably explained by a logarithmically decelerating function with relaxation times varying from days to months [*Marone et al.*, 1991; *Hsu et al.*, 2006; *Ingleby and Wright*, 2017]. Distributed deformation of the viscoelastic medium appears as a more diffuse and long-wavelength signal in the data. The temporal evolution of this signal is not well explained by the exponentially decaying solution expected from a spring-dashpot analysis; the early relaxation is rapid, occurring over months, and is then followed by a much slower relaxation process [*Freed and Bürgmann*, 2004; *Freed et al.*, 2010; *Bürgmann and Dresen*, 2008]. Studies that attempt to fit the observations from the first year or so of postseismic relaxation following $M_w \sim 7$ earthquakes find

relaxation times on the order of 1 year, whereas estimates from later time periods show relaxation times of 10 years or more. An additional key observation from the postseismic period is that afterslip is typically observed or inferred for earthquakes down to $M \sim 3$ [*Ingleby and Wright*, 2017; *Alwahedi and Hawthorne*, 2019; *Hawthorne et al.*, 2016; *Chen and Lapusta*, 2009], but it has been exceedingly challenging to observe a notable viscoelastic signal following earthquake ruptures of $M_w < 7$.

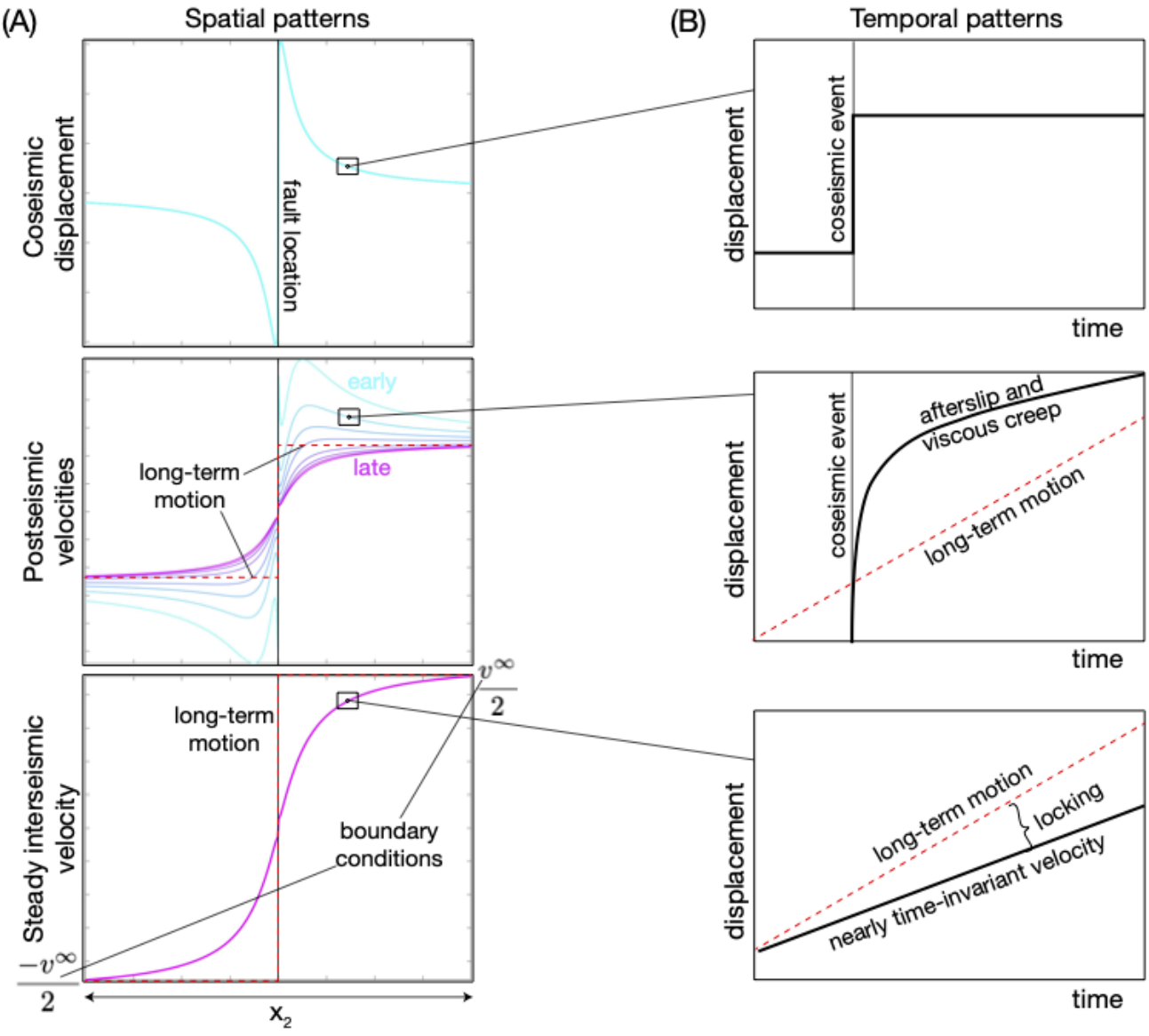

Figure 1: Schematic displacement and velocity evolution recorded at the Earth's surface over the entire earthquake cycle. We show both, (A) the spatial pattern (in colours varying from blue - early postseismic, to pink - late postseismic) and (B) the temporal evolution at a chosen location (black lines). The geodetic predictions from steady rigid block motion is shown in red dashed lines, and deviations from this motion arise due to effects of the earthquake cycle.

1.3 The underlying physical and computational problem

The goal is to infer the rheology of the fault and surrounding medium from the spatio-temporal pattern of surface deformation that contain the features described in the previous section. Two predominant modeling strategies are used for such studies - kinematic modeling of the deformation field and parameter estimation using dynamic models.

1.3.1 Kinematic models

Kinematic models use principles of linear elasticity to develop an impulse-response type relationship between unit inelastic shear and displacements at the Earth's surface [e.g., *Segall*, 2010]. This set of linear relationships is then used to construct a set of normal equations to estimate slip or strain distributions within the discretized domain to explain the data. The results of such an exercise are estimates of the inelastic source deformation (fault slip - $\Delta s(t)$ and distributed strain - $\Delta\varepsilon(t)$), which then may be combined with elastic stress computations to estimate the constitutive relationship between stress change and incremental slip/strain and other derivative quantities.

1.3.2 Dynamic models

Dynamic models take an alternative forward modelling approach, whereby equations of motion are used to solve for the time-dependent bulk and surface deformation arising from an underlying source process, which itself may be explicitly modeled to be time-dependent. These dynamic models typically perform physics-based simulations to solve for the stress (σ) and strain-rate evolution ($\dot{\varepsilon}$) consistent with quasistatic equilibrium: $\nabla \cdot \sigma(\dot{\varepsilon}) + \mathrm{f}_b = 0$. f_b is the equivalent body force applied to the system, which could arise from gravity or imposed slip and tractions as a boundary condition [e.g., *Segall*, 2010]. The constitutive relations i.e., σ as a function of $\dot{\varepsilon}$, along with knowledge of the initial and boundary conditions can be used to compute the evolution of deformation at the observational sites on the surface of the Earth and an optimization may be performed to estimate the best-fit coefficients relating σ and $\dot{\varepsilon}$.

The boundary conditions for this system generally correspond to Dirichlet boundaries at the lateral edges of the domain (either zero or fixed plate motion depending on how the data is decomposed), and traction-free boundaries at the vertical edges (e.g., Figure 2A). The initial conditions are thought to strongly control the behaviour of the system, and generally come from an estimate of the pre-earthquake velocities or strain rates in the system and an imposed stress perturbation from the coseismic event. Some modeling strategies treat the pre-earthquake strain rate as a free parameter that is also estimated as part of the inverse problem.

1.3.3 Decomposing the time series

To simplify the inverse problem, many kinematic and dynamic modeling studies decompose the observed tectonic deformation time series into additive contributions arising from (1) a constant in time but spatially variable velocity field and (2) residual terms that are supposed to correspond to time-dependent postseismic deformation (Figure 1). This simplification helps split the spatial domain of the problem into a computationally convenient framework - by neglecting the spatially variable velocity field, post-earthquake relaxation studies need only model inelastic deformation sources that satisfy a zero-displacement boundary condition; a condition that is satisfied trivially for a finite deformation source. A point to note is that this linear decomposition of the timeseries holds exactly for kinematic methods as well as dynamic models that employ a linear rheology, but can be a source of error and bias if the rheology is non-linear.

1.3.4 Viscoelastic earthquake cycle models

To circumvent issues related to far-field boundary and initial conditions, as well as data decomposition, numerical studies can focus on periodic earthquake cycles. These class of models have been developed in an effort to predict and explain time-dependent earthquake cycle deformation consistent with not only a single earthquake, but the cumulative effects of periodic earthquake sequences integrated over time (across 10's or 100's of earthquakes) to reach an approximately cycle invariant state.

Analytic and semi-analytic interseismic velocity models have been developed assuming linear viscoelastic rheologies in both the cases of a finite thickness faulted elastic layer over an unbounded viscoelastic region [*Savage and Prescott*, 1978; *Cohen and Kramer*, 1984; *Hetland and Hager*, 2005, 2006], depth-averaged rheology models [*Lehner and Li*, 1982; *Li and Rice*, 1987; *Spence and Turcotte*, 1979], as well as a thin viscoelastic channel [*Cohen and Kramer*, 1984]. These models use linear Maxwell or Burger's rheologies [*Hetland and Hager*, 2005] to describe the viscoelastic medium and assume that earthquakes rupture the entire elastic layer. More recent studies account for the mechanical coupling between afterslip and viscoelastic deformation. Since these models involve linear rheologies, the effect of velocity boundary conditions is weak, and the inverse exercise simply involves fitting the curvature in the data with an optimum value of the viscosity (or viscosities for a Burger's body) of the system.

An alternative approach is to incorporate rheological parameterizations based on laboratory experiments when solving for equilibrium conditions. These laboratory-derived rheological models are typically determined from studies of single crystal or polycrystal assemblages of minerals thought to be the dominant deforming phase in the crust (quartz) and mantle (olivine) [*Hirth*, 2002; *Hirth and Kohlstedt*, 2003]. These flow laws are then evaluated at values determined from geological estimates of compositional and thermal variations within the lithosphere to derive rock rheologies at the kilometer scale [*Lyzenga et al.*, 1991; *Reches et al.*, 1994; *Takeuchi and Fialko*, 2012, 2013]. Recent numerical studies have incorporated viscoelastic deformation in simulations of earthquake sequences along a strike-slip fault setting, providing a self-consistent framework that can reproduce all aspects of the earthquake cycle, including spontaneous earthquake nucleation, propagation and arrest [*Lambert and Barbot*, 2016; *Allison and Dunham*, 2017, 2021].

Both classes of numerical simulations pose their own challenges. Linear viscoelastic models are borne out of computational simplicity and are able to fit many aspects of postseismic deformation, however they predict late interseismic locking depths that are significantly deeper than the brittle-ductile transition and are limited in their ability to match observations [e.g., *Takeuchi and Fialko*, 2012]. Numerical simulations that make use of more sophisticated laboratory-derived flow laws are more numerically challenging and computationally expensive [e.g., *Lambert and Barbot*, 2016]. While they are able to better explain observations over the entire period between earthquakes, their relatively high computational expense poses a challenge for coupling them into an observational data-driven optimization problem, limiting their current utility for exploring and identifying effective constitutive relations of the lithosphere. Thus, there is need for a class of simulations that both satisfies the plate motion-derived kinematic boundary conditions and enables efficient exploration of various rheological parameterizations in order to evaluate what constraints may be afforded from surface deformation data on the effective rheology of the lithosphere.

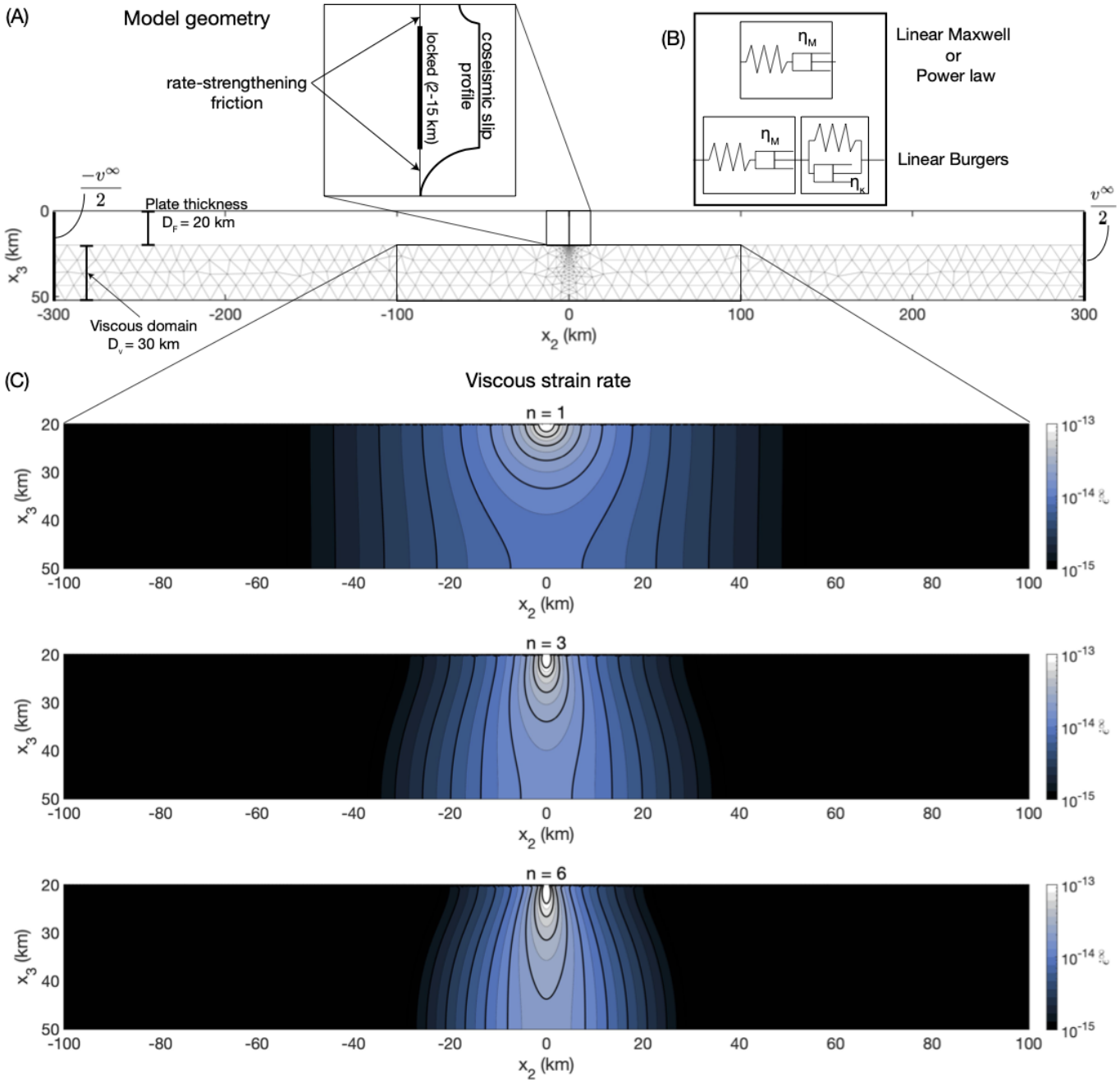

Figure 2: (A) Geometry of the numerical experiments. The domain of the stress calculations are separated into an elasto-frictional domain from 0-20 km depth and a viscoelastic domain from 20-50 km depth. Shear resistance in the frictional domain is given by rate-state friction, while the viscoelastic domain is governed by either a Maxwell rheology (the dashpot can be linear or power-law) or a linear Burgers rheology. (B) These rheologies are shown schematically. η_M - Maxwell viscosity, η_k- Kelvin viscosity. (C) Long-term viscous strain rate $\left(\sqrt{\left(\dot{\varepsilon}_{12}^{\infty}\right)^2+\left(\dot{\varepsilon}_{13}^{\infty}\right)^2}\right)$ as a function of the power exponent n.

1.4 Aim of this study

In this article we discuss using earthquakes and the related cycle of loading and stress release, in an idealized two-dimensional strike-slip fault geometry, to study the rheological properties of the lithosphere. The aim is to develop numerical models of periodic earthquake cycles that satisfy the applied boundary conditions in the long-term (integrated over many earthquake cycles) as well as mechanical equilibrium throughout the earthquake cycle. We qualitatively compare the predictions from our simulations with observations from strain-rate regimes that are orders of magnitude apart, i.e., the interseismic period ($\dot{\varepsilon} < \dot{\varepsilon}^{\infty}$) and the postseismic period ($\dot{\varepsilon} \geq 10\dot{\varepsilon}^{\infty}$), where $\dot{\varepsilon}^{\infty}$ refers to the steady-state strain rate of the system or the strain rate averaged over geological timescales (~ 1 Ma).

We do not attempt to solve for a best-fit rheological description like one would in an inverse problem sense. Instead, we show that linear viscoelastic rheologies need different parameters to explain the interseismic and postseismic periods of the earthquake cycle, as can be modelled by a Burgers rheology [e.g., *Hearn and Thatcher*, 2015], while steady state power-law rheologies with power exponent $n \geq 3$ are able to simultaneously explain the observed localization of strain preceding great earthquakes on mature faults, as well as the typical curvature observed in postseismic deformation timeseries.

2 Methods

Our numerical model is developed in an anti-plane geometry i.e., displacements are only in the out-of-plane x_1 direction, while displacement gradients exist in the $x_2 \times x_3$ plane. We consider a faulted elastic plate supported by a visco-elastic substrate subject to imposed boundary conditions. The thickness of the elastic plate is D_{F}, while the viscous substrate extends from $[D_{\mathrm{F}}, D_{\mathrm{F}} + D_{\mathrm{V}}]$. The elastic plate extends infinitely in the x_2 direction, and the viscous domain is chosen to be large enough to approximate this infinite x_2 extent (Figure 2A).

The boundary conditions for the simulations we run depend on the timescale of the problem i.e., we split the problem into a viscous boundary-value problem for the long-term simulation, and a set of Boundary Integral Equations to simulate the earthquake cycle [*Mallick et al.*, 2021].

2.1 Long-term viscous strain rate

The governing equation for the viscous boundary-value problem is posed in terms of the scalar velocity field $v(x_2, x_3)$,

$$\nabla^2 v(x_2, x_3) = -\left(\frac{\partial \log \eta}{\partial x_2} \frac{\partial v(x_2, x_3)}{\partial x_2} + \frac{\partial \log \eta}{\partial x_3} \frac{\partial v(x_2, x_3)}{\partial x_3} \right) \tag{1}$$

where rheology of the substrate is described as follows,

$$\frac{1}{\eta} = A \left(\sqrt{\sigma_{12}^2 + \sigma_{13}^2} \right)^{n-1} ; \quad \sigma_{1i} = \eta \dot{\varepsilon}_{1i} = \eta \left(\frac{1}{2} \frac{\partial v}{\partial x_i} \right) \tag{2}$$

A is a rheological constant, n is the power in the power-law relation $\dot{\varepsilon} = A\sigma^n$, η is the viscosity and the individual stress components are σ_{1i}.

2.1.1 Boundary conditions and solution

The boundary conditions on this system are as follows: traction-free at the base ($\sigma_{13}\,(x_3 = D_\mathrm{F} + D_\mathrm{V}) = 0$); lateral edges are subject to anti-symmetric Dirichlet boundaries $\left(v\,(x_2 \to \pm\infty) = \pm\frac{v^\infty}{2}\right)$; the entire fault slips uniformly at v^∞ resulting in rigid block-like motion of the elastic layer ($0 \le x_3 \le D_F$).

There exist analytical solutions to this system, as least for spatially uniform values of A, n [*Moore and Parsons*, 2015]. The viscous strain rates for a choice of power-law rheology only depend on n (Figure 2C) and weakly depend on the dimensions of the system. We present these solutions in terms of rescaled dimensions x_2', x_3', where $x_3' = \frac{x_3 - D_\mathrm{F}}{D_\mathrm{V}}$ and $x_2' = \frac{x_2}{D_\mathrm{V}}$. The domain for the solutions are $0 \le x_3' \le 1, -\omega \le x_2' \le \omega$. We choose the aspect ratio $\omega = 10$, which is sufficiently large such that there are negligible effects due to the location of the boundary on the strain-rate tensor [*Moore and Parsons*, 2015].

$$
\begin{aligned}
\frac{\dot{\varepsilon}_{12}^\infty}{v^\infty} &= \frac{1}{2\omega} + \frac{1}{\omega}\left(\sum_{m=1}^{\infty} \frac{\cosh\frac{m\pi(1-x_3')}{\omega\sqrt{n}}}{\cosh\frac{m\pi}{\omega\sqrt{n}}} \cos\frac{m\pi x_2'}{\omega\sqrt{n}}\right) \\
\frac{\dot{\varepsilon}_{13}^\infty}{v^\infty} &= -\frac{1}{\omega\sqrt{n}}\left(\sum_{m=1}^{\infty} \frac{\sinh\frac{m\pi(1-x_3')}{\omega\sqrt{n}}}{\cosh\frac{m\pi}{\omega\sqrt{n}}} \sin\frac{m\pi x_2'}{\omega\sqrt{n}}\right)
\end{aligned}
\tag{3}
$$

We remind the reader that $\dot{\varepsilon}$ refers exclusively to the viscous component of the strain rate. The total strain rate, which is a sum of the viscous and elastic components, is denoted as $\dot{\varepsilon}_\mathrm{total} = \dot{\varepsilon} + \dot{\varepsilon}_\mathrm{elastic}$.

2.2 Periodic earthquake cycle simulations

The steady-state solutions for long-term viscous creep rate (Equation 3, Figure 2C) can be used to compute an equivalent background stressing rate to load earthquake cycle simulations [*Mallick et al.*, 2021]. We note that without the long-term strain rates, one would have to assign a spatially variable long-term slip rate and strain rate to drive the earthquake cycle simulations [e.g., *Lambert and Barbot*, 2016], but this would not necessarily satisfy the boundary conditions of the system.

Using a background stressing rate that is kinematically and dynamically consistent with the long-term boundary conditions, we transform the time-dependent partial differential equations for quasi-static equilibrium to a set of coupled ordinary differential equations [e.g., *Lambert and Barbot*, 2016; *Mallick et al.*, 2021]. Here we discuss the procedure in brief; we discretize the non-elastically deforming part of the domain using constant-slip boundary elements for faults and constant-strain boundary elements for viscous shear. These boundary elements along with Equation 3 can be used to compute the long-term loading rate of the system as follows,

$$
\begin{bmatrix} \dot{\sigma}_F^\infty \\ \dot{\sigma}_{12}^\infty \\ \dot{\sigma}_{13}^\infty \end{bmatrix} = \begin{bmatrix} K_{F,F} & K_{F,12} & K_{F,13} \\ K_{12,F} & K_{12,12} & K_{12,13} \\ K_{13,F} & K_{13,12} & K_{13,13} \end{bmatrix} \begin{bmatrix} -v^\infty \\ -\dot{\varepsilon}_{12}^\infty \\ -\dot{\varepsilon}_{13}^\infty \end{bmatrix}
\tag{4}
$$

$K_{a,b}$ is a stress-interaction kernel or the boundary-element approximation of the Green's function tensor that describes the elastic stress transfer to any given element a in response to inelastic shear (slip on faults and strain in shear zones) on the considered element b [*Barbot*, 2018].

Deviations from the long-term loading rate (Equation 4) drive frictional slip and viscous shear within the computational domain over the earthquake cycle. The set of coupled ordinary differential equations we need to solve is therefore the instantaneous momentum balance for each

boundary element [e.g., *Mallick et al.*, 2021]. To do this, we account for the full elastic interaction between each point on the fault and in the viscous shear zones using the above described stress interaction kernel .

$$\begin{bmatrix} K_{F,F} & K_{F,12} & K_{F,13} \\ K_{12,F} & K_{12,12} & K_{12,13} \\ K_{13,F} & K_{13,12} & K_{13,13} \end{bmatrix} \begin{bmatrix} v - v^{\infty} \\ \dot{\varepsilon}_{12} - \dot{\varepsilon}_{12}^{\infty} \\ \dot{\varepsilon}_{13} - \dot{\varepsilon}_{13}^{\infty} \end{bmatrix} = \begin{bmatrix} \frac{\mathrm{d}\sigma_{\text{friction}}}{\mathrm{d}t} \\ \dot{\varepsilon}_{12}\frac{\mathrm{d}\eta}{\mathrm{d}t} + \eta\frac{\mathrm{d}\dot{\varepsilon}_{12}}{\mathrm{d}t} \\ \dot{\varepsilon}_{13}\frac{\mathrm{d}\eta}{\mathrm{d}t} + \eta\frac{\mathrm{d}\dot{\varepsilon}_{13}}{\mathrm{d}t} \end{bmatrix} \tag{5}$$

The left hand side of this set of equations is the stressing rate in the system arising from elasticity while the right hand side is the time derivative of the shear resistance provided by the rheology of the fault zone and viscoelastic medium. Details about the chosen rheologies are provided in the following section.

2.2.1 Friction and viscous laws

Resistive strength evolution on the fault (Equation 5) is described by rate-dependent friction [*Marone et al.*, 1991] i.e., the resistive strength of the fault is given by $f\sigma_n$ where f is the friction coefficient and σ_n is the effective normal strength on the fault, and reference values f_0, v_0.

$$\sigma_{\text{friction}} = f(v)\sigma_n = \left(f_0 + (a-b)\log\frac{v}{v_0}\right)\sigma_n \tag{6}$$

The rheological models we test in the viscoelastic domain are the linear Maxwell, linear Burgers and power-law rheologies (Figure 2B). The total strain rate in these rheologies are of the form,

$$\dot{\varepsilon}_{\text{total}} = \frac{\dot{\sigma}}{G} + \frac{\sigma}{\eta_M} + \dot{\varepsilon}_k \begin{cases} \dfrac{\sigma - G\varepsilon_k}{\eta_k}, & \text{Burgers body} \\ 0, & \text{otherwise} \end{cases} \tag{7}$$

where $\dot{\varepsilon}_k$ is the Kelvin strain only present for a Burgers body, η_M is the viscosity of the Maxwell element (for power-law rheologies, η_M in turn is a function of $\dot{\varepsilon}$ i.e., $\frac{\mathrm{d}\eta}{\mathrm{d}t} \neq 0$ in Equation 5) and G is the elastic shear modulus of the system.

To study the role of viscous rheology in modulating the stress state in this system, and the associated displacement and velocity field at the free surface, we vary the two parameters used to describe the rheology in the viscous shear layer for the spring-dashpot bodies (linear Maxwell and power-law): A, n; while we vary the Kelvin and Maxwell viscosities for the Burgers material: η_k, η. We also vary the recurrence time for the earthquake to see how relaxation in the lithosphere is related to the magnitude of coseismic stress perturbation. We list model parameters we varied for these simulations in Table 1.

2.2.2 Initial conditions from coseismic slip

The set of ordinary differential equations we need to solve is Equation 5 in terms of the variables $[v, \dot{\varepsilon}_{12}, \dot{\varepsilon}_{13}]$, subject to the rheologies in Equation 6-7. To guarantee a unique solution for this system, we need to determine the initial condition for $[v, \dot{\varepsilon}_{12}, \dot{\varepsilon}_{13}]$. This is done by using the stress change due to prescribed coseismic slip on the fault to instantaneously change values of $[v, \dot{\varepsilon}_{12}, \dot{\varepsilon}_{13}]$ subject to their rheological properties [*Montési*, 2004]. We prescribe coseismic slip as a uniform value of $u^{\infty} = v^{\infty}T_{eq}$ within the locked domain (2-15 km), and tapered in the surrounding section of fault such that the stress increase does not exceed 3 MPa and slip within this domain is minimized

Table 1: Model parameters for earthquake cycle simulations

Parameter	Range
Fault width	20 km
x_3 scale	30 km
x_2 scale	200 - 500 km
Shear modulus (G)	30 GPa
T_{eq}	50, 100, 200 yrs
v^{∞}	10^{-9} m/s
Viscous layer (linear Maxwell, power-law)	
Δx	variable mesh size
n	$1, 2, 3, 4, 5, 6$
A^{-1}	$10^{18}, 3\times10^{18}, 7\times10^{18}, 10^{19}, 5\times10^{19}, 10^{20}$
Viscous layer (linear Burgers)	
Δx	variable mesh size
η_M (Pa-s)	$10^{18}, 5\times10^{18}, 10^{19}, 5\times10^{19}, 10^{20}$
η_k (Pa-s)	$5\times10^{17}, 10^{18}, 5\times10^{18}$
Fault parameters	
Δx_3	500 m
$a-b$	0.015
σ_n	40 MPa
f_0, v_0	0.6, 10^{-6} m/s

(Figure 2A). This is a linear inequality constrained optimization that is done using the MATLAB function *lsqlin*.

With the initial conditions determined from coseismic slip, we integrate the system of equations using MATLAB's Runge-Kutta fourth order solver *ode45* to obtain the time history of $[v, \dot{\varepsilon}_{12}, \dot{\varepsilon}_{13}]$ over the entire domain. Since the coseismic slip derived initial conditions only provide a change in the integrable variables, we need to run these earthquake cycles a number of times until we obtain cycle invariant results [e.g., *Hetland and Hager*, 2005; *Takeuchi and Fialko*, 2012]. In that case, the coseismic slip derived stress change is imposed every T_{eq} years. We find that, depending on rheology, 10-20 cycles is sufficient to obtain cycle invariant results given the rheological parameters and timescales we have chosen.

2.3 Parameters that can be estimated geodetically

We consider two main parameters that can be inferred geodetically that are generally used to describe the period following and leading up to large plate boundary earthquakes. In the postseismic period we estimate the effective relaxation time of the system, t_R; we describe the interseismic signal using an effective locking depth, D_{lock}.

For postseismic relaxation, we consider only the deviation from steady state behaviour i.e., we remove displacements associated with the long-term motion of the plate boundary or the steady-state strain rates ($\dot{\varepsilon}^{\infty}_{12}, \dot{\varepsilon}^{\infty}_{13}$). We characterize the transient surface displacements during the first 2 years following the earthquake using a two step procedure. First we use singular-value decomposition on the displacement timeseries and extract the temporal component associated

with the most dominant singular value. We fit this with the following functional form,

$$u(t) = \beta\left(1 - \exp\left(-t/t_R\right)\right) \tag{8}$$

The estimated value of t_R gives the best-fit relaxation time of the system over the observational window [*Perfettini and Avouac*, 2004].

Later in the earthquake cycle, we consider the interseismic period as the time period when the maximum surface velocity is smaller than the relative plate velocity i.e., $|v(x_2)| \leq \frac{v^\infty}{2}$. The resulting velocity field can then be fit to an arc-tangent function [*Savage and Burford*, 1973],

$$v(x_2) = \frac{v^\infty}{\pi}\tan^{-1}\left(\frac{x_2}{D_{lock}}\right) \tag{9}$$

The estimated locking depth controls the effective width of the surface that is experiencing interseismic strain, and is thus a physically motivated representation of the spatial pattern of the signal.

3 Results

We describe the surface deformation observations predicted at geodetic sites over the entire earthquake cycle, as well as the corresponding strain rate evolution within the viscoelastic domain from our numerical experiments (Figure 3, 4). Since we are interested in cycle invariant behaviour, we only present results from the last earthquake cycle; the previous cycles are necessary only for spin up. The results are discussed separately for linear Maxwell, linear Burgers and power-law rheologies in terms of interseismic locking depths (Figure 5), cumulative postseismic displacements (Figure 6) and effective relaxation timescales (Figure 7).

3.1 Linear Maxwell

For linear Maxwell rheologies, both the amplitude and effective relaxation timescale of the postseismic response directly depend on the viscosity (η_M). As η_M increases, the timescale for stress relaxation following the coseismic perturbation (t_R) increases, while the magnitude of the initial jump in strain rate $(\Delta\dot{\varepsilon}(\Delta t = 0))$ decreases.

$$\begin{aligned} t_R &= \frac{\eta_M}{G} \\ \Delta\dot{\varepsilon}_M(\Delta t = 0) &= \frac{\Delta\tau_{co}}{\eta_M} \approx \frac{K\left(v^\infty T_{eq}\right)}{\eta_M} \end{aligned} \tag{10}$$

A dominant feature from simulations incorporating a linear Maxwell rheology is that they show strain rates that are diffusive is space and in time (Figure 3A). The initial strain rate following the earthquake decays in space as expected from the stress change $\Delta\tau_{co}$. In time, the elevated strain rate is damped as it diffuses outwards. At the end of the earthquake cycle $(\Delta t/T_{eq} \to 1)$, nearly the entire viscoelastic medium is at a uniform strain rate level and the resulting surface velocity field appears to have a near constant spatial gradient (Figure 4D).

Many aspects of the evolution of this viscoelastic system can be explained by a single dimensionless variable, $\tau_M = \frac{T_{eq}}{2t_R} = \frac{GT_{eq}}{2\eta_M}$ [*Savage and Prescott*, 1978; *Savage*, 2000]. Models with $\tau_M >> 1$ generate relatively large magnitude postseismic deformation early in the earthquake cycle and predict relatively small near fault velocity gradients late in the earthquake cycle. Conversely, if

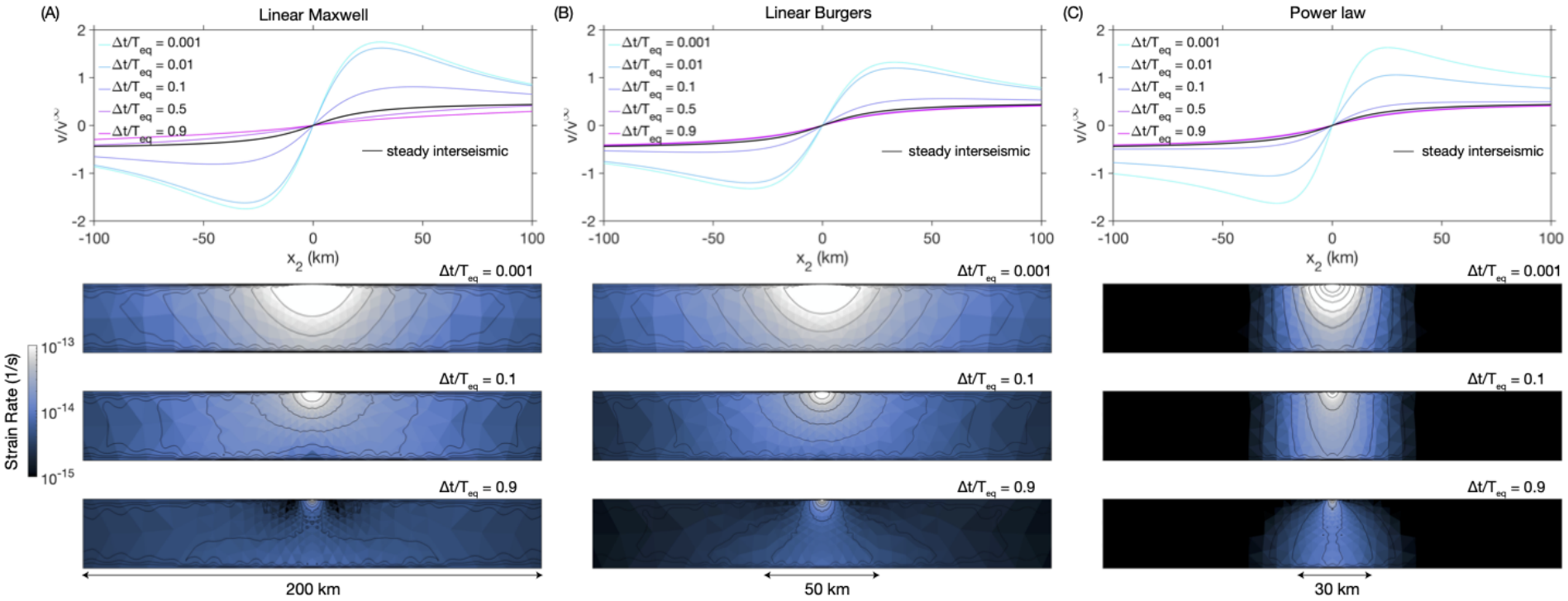

Figure 3: Surface velocity and internal viscous strain rate evolution over the earthquake cycle for different rheologies for a periodic earthquake cycle of $T_{eq} = 50$ years. The rheologies were chosen such that the early postseismic surface velocity field is nearly identical. (A) Linear Maxwell body ($\eta_M = 3 \times 10^{18}$ Pa-s), (B) Linear Burgers body ($\eta_k = 3 \times 10^{18}$ Pa-s, $\eta_M = 5 \times 10^{19}$ Pa-s) and (C) Power law rheology ($A^{-1} = 3 \times 10^{18}$, $n = 3$). The linear rheologies allow accelerated viscous deformation of significantly larger volume of material compared to the power-law rheology, which promotes localization of strain. This effect is noticeable in all the strain rate snapshots.

$\tau_M << 1$, the model behavior approaches the elastic limit where there is negligible viscous response and the predicted surface velocities vary only moderately around the steady state elastic expectation throughout the earthquake cycle.

3.1.1 Interseismic locking depth

Systems characterized by large τ_M, which could arise from large T_{eq} or small t_R, result in large locking depths at the end of the interseismic period while low τ_M systems show significantly smaller locking depths (Figure 5A-B). An additional feature is that the estimated locking depth in these simulations increases monotonically in time, with the amplitude of this time-dependence directly related to τ_M (Figure 5D).

3.1.2 Postseismic creep and relaxation time

Postseismic velocities following an earthquake decay exponentially for linear Maxwell bodies beyond a short, initial acceleration period. This acceleration period scales with the logarithm of η_M. The time constant for the subsequent decay is the relaxation time of the system (t_R), and it is a material property (Figure 6). As a result, T_{eq} does not affect the estimated t_R value or the spatial pattern of postseismic deformation (Figure 6,7).

3.2 Linear Burgers

The linear Burgers rheology is characterized by two separate timescales: a short-term anelastic timescale $\frac{\eta_k}{G}$ controlled by the viscosity of the Kelvin element, and a long-term Maxwell timescale $\frac{\eta_M}{G}$ (assuming $\eta_k < \eta_M$) [*Müller*, 1986; *Hetland and Hager*, 2005]. Only the creep associated with the Maxwell element is recorded as permanent strain, the anelastic term is significant for geodetic observations but does not leave a record in the long-term.

Similar to the linear Maxwell case, the linear Burgers body also exhibits a tendency to diffuse strain rate away from the fault with time (Figure 3C). This pattern depends on three variables - T_{eq}, and the two relaxation times associated with η_k and η_M. Large values of η_k, η_M resemble an elastic medium, and small values of T_{eq} lead to small stress perturbations and hence minimal deviation from a time-invariant steady-state model. Small values of η_k and η_M, or large values of T_{eq} lead to more pronounced earthquake cycle effects. The effects of these quantities can be understood by examining the instantaneous strain rate change in the Kelvin and Maxwell elements due to coseismic slip.

$$\begin{aligned} \Delta\dot{\varepsilon}_k(\Delta t = 0) &\approx \frac{K\left(v^{\infty} T_{eq}\right)}{\eta_k} \\ \Delta\dot{\varepsilon}_M(\Delta t = 0) &\approx \frac{K\left(v^{\infty} T_{eq}\right)}{\eta_M} \end{aligned} \tag{11}$$

The subsequent relaxation follows an initial relaxation controlled by η_k which then smoothly transitions to the relaxation timescale of η_M. The transition timescale is controlled by the ratio of $\frac{\eta_k}{\eta_M}$ [*Hetland and Hager*, 2005]. While we do not consider scenarios of $\frac{\eta_k}{\eta_M} > 1$ in our simulations, the reduction of a Burgers system to a Maxwell body is possible by increasing $\frac{\eta_k}{\eta_M} \to \infty$ since at that limit there is no transient strain in the Kelvin element anymore.

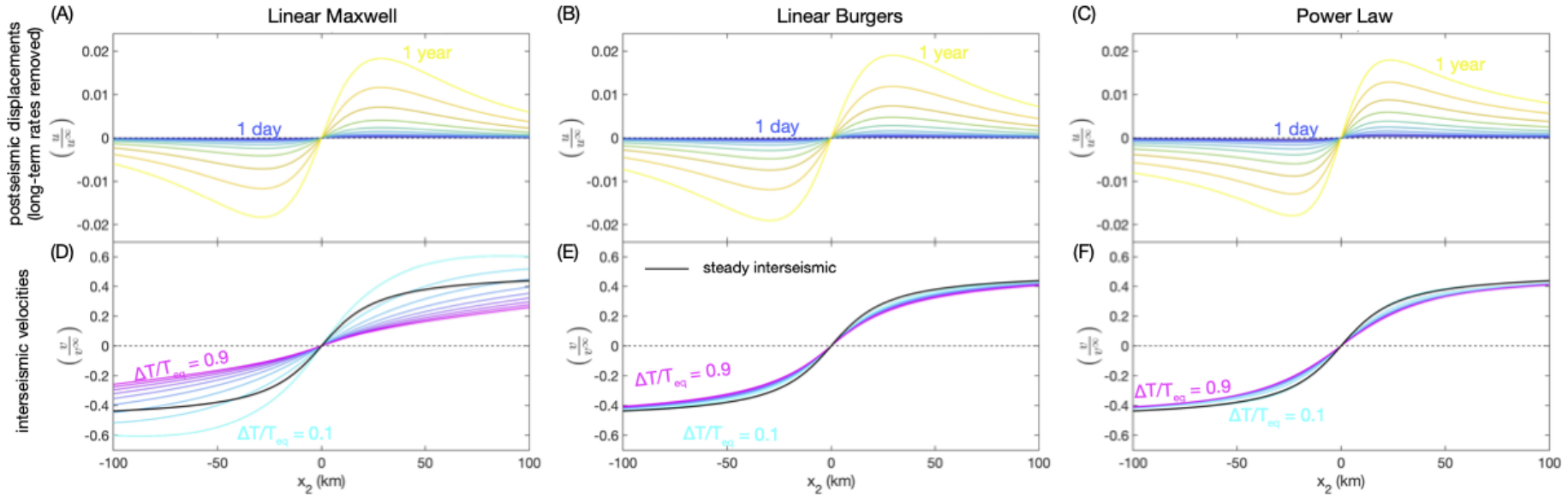

Figure 4: Surface predictions of postseismic displacements and interseismic velocities for different rheologies for a periodic earthquake cycle of $T_{\text{eq}} = 100$ years. The rheologies are chosen such that the cumulative postseismic after 1 year is nearly identical for all three models. (A)-(C) Cumulative postseismic displacements normalized by the coseismic slip amount $\left(u^{\infty} = v^{\infty} T_{\text{eq}}\right)$ for times varying from 1 day to 1 year. (D)-(F) Interseismic velocities compared to the steady interseismic expectation (black line).

3.2.1 Interseismic locking depth

Late interseismic locking depths show systematic dependence on only two parameters - η_M and T_{eq} (Figure 5C). η_k controls the early postseismic response but does not contribute to the late interseismic behaviour. Larger η_M produces smaller locking depths while increasing T_{eq} increases the locking depths, which suggests that late interseismic behaviour of this system is controlled by the same dimensionless parameter as the linear Maxwell case, $\tau_M = \frac{GT_{eq}}{2\eta_M}$ [*Savage and Prescott*, 1978; *Savage*, 2000]. The estimated locking depth for simulations with small effective τ_M, due to low T_{eq} or large η_M, are comparable to a purely frictional-elastic simulation and show a nearly time-invariant behaviour (Figure 5D).

3.2.2 Postseismic creep and relaxation time

Linear Burgers bodies do not have a single relaxation timescale, and thus our estimates of t_R depend on the time window that is considered. However, this relaxation timescale is independent of the coseismic slip magnitude and thus has no dependance on T_{eq}. We consider a 2-year time window, which is a typical observational window used in geodetic studies, in order to estimate the relaxation time and effective viscosity of the system. In most of our simulations, this estimated relaxation time corresponds to sampling the viscous relaxation controlled by η_k. Higher values of η_k lead to larger relaxation times, with the effect of η_M being negligible for the 2-year observational window and the parameter range we considered (see caption in Figure 6).

3.3 Power-law

Our numerical experiments governed by power-law rheologies are characterized by two main features - (1) the interseismic locking depths appear to be a constant in time and only weakly sensitive to the parameters we varied (Figure 5A-B), and (2) the postseismic relaxation timescale and amplitude appear to depend on the coseismic slip amplitude and conform poorly to the $\exp(-t/t_R)$ functional form we chose to fit it with (Figure 4C, 7B), i.e., the curvature in the timeseries is closer to a logarithmic decay than the exponential function we chose [e.g., *Montési*, 2004].

3.3.1 Localized deformation and interseismic locking depth

For our simulations with power-law rheologies, deformation throughout the entirety of the earthquake cycle is significantly more localized in space than as observed for the linear viscoelastic rheologies discussed above (Figure 3C). The extent of localization depends on the power exponent n as well as the rheological parameter A. We contrast this with the fact that the solution to the long-term viscous boundary value problem does not depend on A (Equation 3). Thus, our simulation results suggest that both A and n may be inferred from geodetic data by combining insight throughout the entire earthquake cycle.

Larger stress exponents n favor increased localization while large coefficients A reduce the impact of stress perturbations from coseismic slip, similar to how the magnitude of the viscosity of linear rheologies controls the change in strain rates in Equation 10. While the degree of strain localization depends on the power law stress exponent, for the parameter space explored, we find that models with power law exponents $n \geq 3$ exhibit nearly identical late interseismic locking depths (Figure 5A,D), and are generally comparable to simple back-slip models of interseismically locked faults.

3.3.2 Postseismic creep and relaxation time

The postseismic deformation timeseries is not expected to conform to the exponential functional form we used to fit the timeseries. This is because the exponential function is a solution to the linear viscoelastic problem [*Perfettini and Avouac*, 2004,], and the outputs of a power-law rheology correspond to an effective viscosity that systematically increases in time [*Montési*, 2004]. However, since we consider time windows on the order of 1-2 years, the relaxation timescale can be fit using a linear viscoelastic approximation to estimate an average relaxation time over that window. These relaxation timescales are not only dependent on rheological parameters A, n but are a function of the earthquake size, parameterized here in terms of coseismic slip (Figure 6).

For a given set of rheological parameters A, n (for $n > 1$), the cumulative postseismic deformation over a given time window (in this case Δt =2 years), even when normalized by the coseismic slip amount, increases with earthquake size (Figure 7A). The normalized postseismic deformation following small earthquakes in our simulations ($u^{\infty} \sim 1.5$m) amounts to about 30% of the normalized postseismic deformation following the largest earthquakes ($u^{\infty} \sim 12$m). On the other hand, the estimated relaxation timescale decreases with increasing earthquake size (Figure 7B).

4 Discussion

We have developed numerical earthquake cycle experiments in order to test how well popular rheological models are able to qualitatively reproduce different observational features in geodetic studies over the entire interseismic period. Our simulation results illustrate the non-uniqueness of rheological models, and their parameters, in explaining postseismic data alone (Figures 5-7). However, we demonstrate how this non-uniqueness can be mitigated to some extent by incorporating data corresponding to strain accumulation in the late interseismic period (Figure 5). We find that steady-state power-law rheologies with $n \geq 3$ as well as linear Burgers rheology with $\eta_M \approx 10^{20}$ Pa-s and $\eta_k \approx 10^{18}$ Pa-s are able to explain early postseismic relaxation as well as the strain localization observed near strike-slip faults late in the interseismic period. While we do not show it explicitly, nonlinear Burgers rheologies with $n \geq 1$ (with relevant A values) could explain the geodetic data just as well. This is because a steady-state rheology, linear or power-law, is simply a limiting case of an appropriate Burgers rheology where the transient viscosity is much larger than the steady-state value. On the other hand, linear Maxwell rheologies are simply insufficient to explain the observational features.

In the following sections, we first discuss the equivalence between linear Burgers and power-law descriptions of lithospheric rheology for the earthquake cycle, and then detail geophysical observations that may be required to convincingly discriminate between these two rheologies. We then expound on the relationship between inferences of average rheological parameters from crustal scales and those measured in laboratory experiments, and how a power-law rheology is consistent with both geodetic observations and laboratory-derived flow laws. Finally, we conclude with the implications for stress transfer and the associated assessment of regional hazard when frictional and viscous creep are mechanically coupled.

4.1 The effective rheology of the lithosphere

Geodetic investigations of lithospheric rheology, specifically the lower crust and uppermost mantle, that consider only a relatively short time window ($\Delta t < 5$ years) as is typical of geodetic postseismic studies, may not be able to distinguish between any of the rheological models discussed in

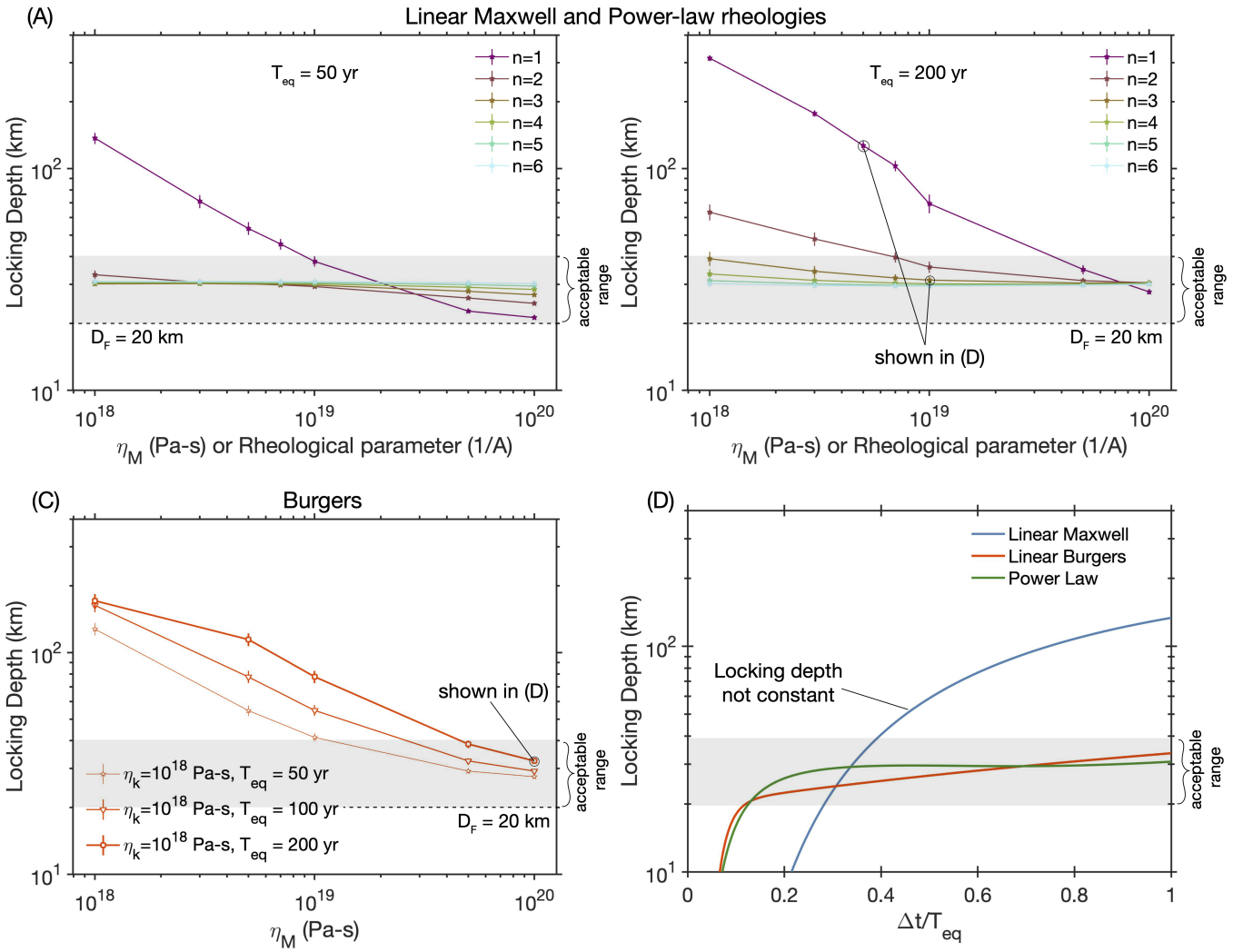

Figure 5: Compilation of late interseismic locking depths for various rheological choices and two different T_{eq}. Locking Depth (assuming an arc-tangent functional fit - $\frac{v^{\infty}}{\pi}\tan^{-1}\frac{x_2}{D}$) for (A) Linear Maxwell and power-law materials with n varying from 1 to 6 for $T_{eq} = 50$ years. (B) Same as (A) for $T_{eq} = 200$ years. (C) Locking depths for a linear Burgers rheology for a constant η_k and varying η_M and T_{eq}. Late interseismic locking depths show no dependence on η_k. (D) The estimated locking depth varying in time over the interseismic period for different rheologies. Both the power-law body and linear Burgers (with large η_M) show nearly time invariant late-interseismic locking depth.

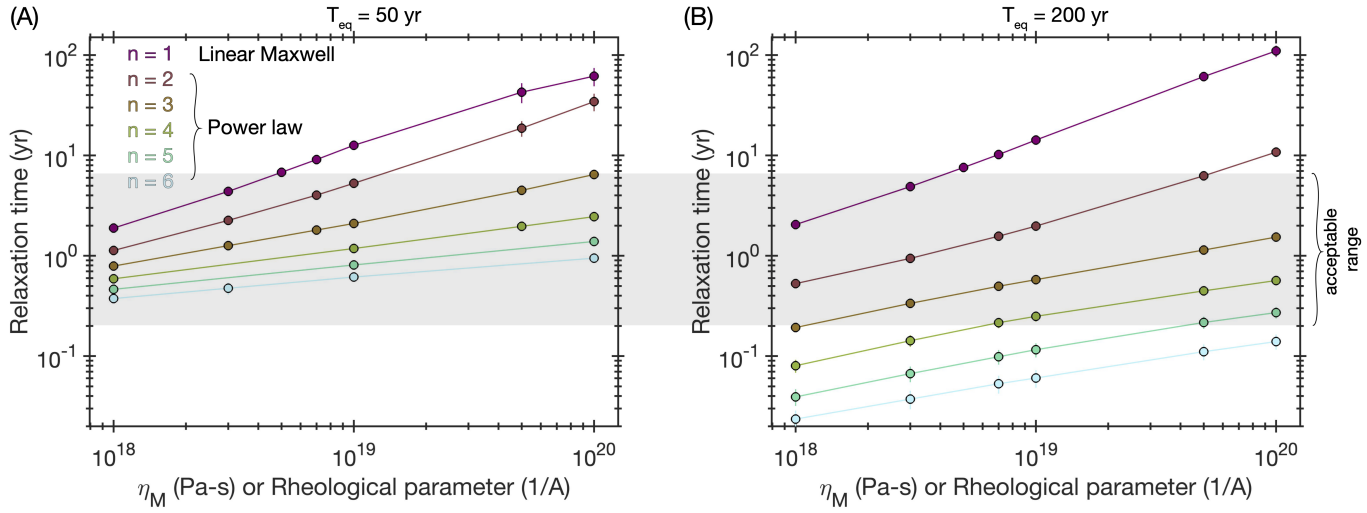

Figure 6: Postseismic relaxation times for linear Maxwell and power law bodies estimated over a 2 year period following the earthquake for a recurrence interval of (A) 50 years and (B) 200 years. Increased T_{eq} leads to larger coseismic slip $\left(u^{\infty} = v^{\infty} T_{eq}\right)$, and hence larger stress change to drive postseismic creep. Linear Maxwell bodies follow a stress-independent relaxation time given by $t_R \approx \frac{\eta_M}{G}$. The relaxation time of power law bodies show a significant reduction for larger coseismic slip. We do not show the results for Burgers bodies since their relaxation times over the given time window are exactly as predicted by the viscosity of the Kelvin element $t_R \approx \frac{\eta_k}{G}$.

this paper (linear Maxwell, linear Burgers and power-law). This is because postseismic geodetic observations can be reduced into two features - a spatial pattern of cumulative postseismic deformation and the effective relaxation timescale (Figure 7), and there exists a non-unique mapping between rheological parameters from each of the discussed rheological models to these spatial and temporal patterns of the deformation data (Figure 7 - 8A-B).

However, the three rheological models display diverging behavior as the observational window gets larger; this is what we exploit during the late interseismic period. Interseismic strain localization and the stationarity of the locking depth in time is observed in models with either a power-law rheology or a linear Burgers rheology that approximates the effective viscosity evolution of a power-law body (Figure 8D). In contrast, linear Maxwell rheologies promote diffuse strain distributions (Figure 3) which manifests as an increase in effective locking depths late in the earthquake cycle (Figure 5D), a feature that is not seen even in the best monitored strike-slip fault systems in the world [e.g., *Hussain et al.*, 2018]. This leads us to suggest that Earth's lithosphere cannot be well-described by a homogenous linear Maxwell body, at least over the timescale of the earthquake cycle.

These findings do not invalidate previous work on estimating the effective viscosity from postseismic, post-glacial and lake rebound deformation observations assuming a linear Maxwell rheology [e.g., *Kenner and Segall*, 2003; *Johnson and Segall*, 2004; *Devries and Meade*, 2013; *Tamisiea et al.*, 2007; *England et al.*, 2013; *Kaufmann and Amelung*, 2000; *Larsen et al.*, 2005]. However, the important implication is that these estimates of the average viscosity, or viscosity structure, are tied to the observational window. This detail becomes apparent when comparing the lithospheric viscosities estimated from processes that occur over different timescales; longer observations windows typically show significantly higher viscosities e.g., the viscosity of the upper mantle estimated following deglaciation (since the Last Glacial Maximum), which represents a 10^4 year observational time window, is between $10^{20} - 10^{21}$ Pa-s [e.g., *Tamisiea et al.*, 2007; *Milne et al.*, 2001] while typical

viscosities estimated in the decade(s) following $M_w > 7$ earthquakes range from $10^{18} - 10^{19}$ Pa-s [e.g., *Kenner and Segall*, 2003; *Pollitz*, 2005; *Ryder et al.*, 2007]. Both power-law and linear Burgers rheologies can help reconcile these apparently disparate viscosity estimates since both processes produce time-dependent viscosities which increase with time since the applied stress perturbation (Figure 8D).

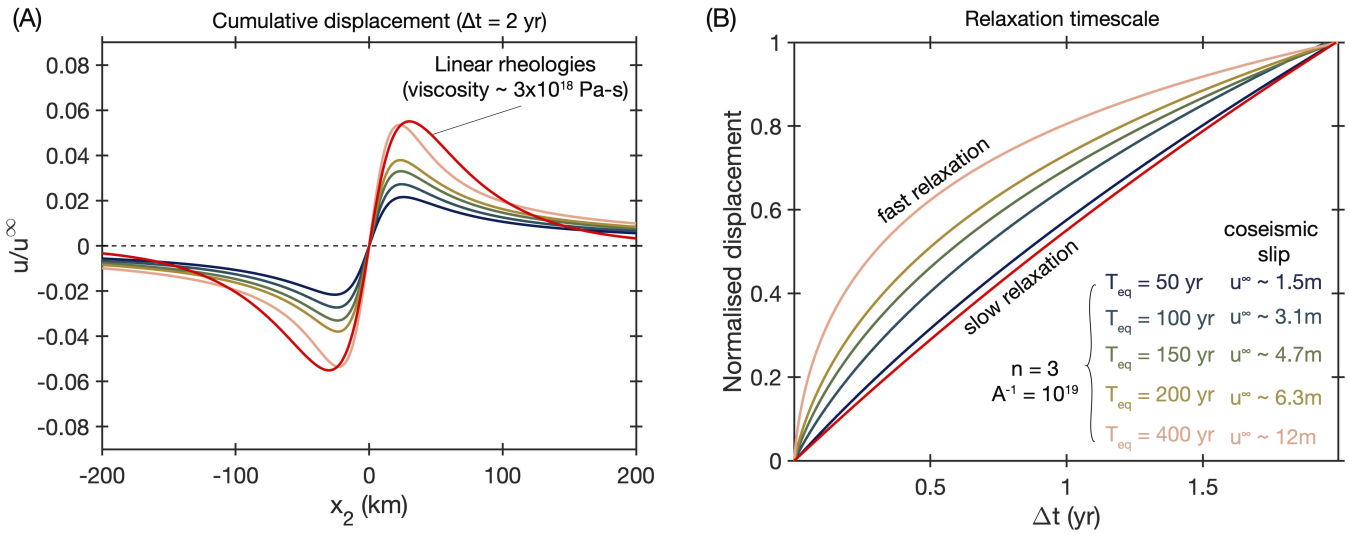

Figure 7: Magnitude dependent postseismic motions for power law bodies. (A) Cumulative postseismic displacement (steady state component removed) normalized by the coseismic slip amount ($u^{\infty} = v^{\infty} T_{eq}$) over 2 years for the same rheology. By increasing the earthquake recurrence interval, we increase the coseismic slip amount. Only power law materials show increasing cumulative deformation with increase in the recurrence interval. (B) As the cumulative deformation increases, the relaxation timescale decreases i.e., the postseismic deformation becomes faster and larger.

4.1.1 Similarities between power-law and linear Burgers rheologies

A question that arises at this point is - how can a linear and power-law rheology satisfactorily explain deformational data throughout the earthquake cycle? The near equivalence between linear Burgers and power-law bodies in our simulations exists because of a non-unique mapping between rheological parameters for each model and the observational features that we use to describe the deformation timeseries (Figure 8A-C).

Consider the viscosity evolution of a power-law body. The power-law rheology results in a lower effective viscosity during the relatively high stress and strain rate postseismic period, and the viscosity gradually increases as stress relaxes and decays to a near time-invariant interseismic state (Figure 8D). The linear Burgers rheology captures this same kinematic behaviour through completely different dynamics. The Burgers description can be thought of as a technique to describe non-steady state viscous rheology i.e., there exists a finite timescale or strain over which the system has to evolve to reach the unique mapping between stress and strain rate [*Müller*, 1986; *Hetland and Hager*, 2005]. In the case of a linear Burgers rheology, the initial low effective viscosity during the postseismic period is a disequilibrium feature that smoothly evolves to its significantly larger steady state viscosity (Figure 8D).

While the overall kinematics predicted by the two different rheological models appear similar, the predictions from the two models are not identical (Figure 8A inset). Although they would

likely be difficult to distinguish after considering the errors and uncertainties in typical geodetic datasets and the various models employed to fit the data [*Duputel et al.*, 2014; *Minson et al.*, 2013].

4.1.2 Magnitude-dependent postseismic motions

Our simulation results suggest that linear Burgers and power-law rheologies may in principle be distinguished by the sensitivity and rate of the postseismic moment release to the magnitude of the coseismic event. For a typical time window ($\Delta t = 2$ yrs), linear viscoelastic rheologies result in postseismic surface deformation that is a linear function of the coseismic slip $\left(u^{\infty} = v^{\infty} T_{\mathrm{eq}}\right)$, and thus can be normalized to produce a constant shape (Figure 7A). Similarly, the temporal evolution of this moment release is invariant of the size of the earthquake (Figure 7B). In contrast, power-law rheologies show a clear magnitude dependence, where the normalized postseismic deformation at the surface is smaller for small events and grows larger with increasing coseismic slip (Figure 7A). The temporal evolution of moment release is also a function of event size with smaller events having much slower relaxation than larger events (Figure 7B).

While this magnitude-dependent behaviour has not been studied thoroughly, there is some evidence to suggest the existence a magnitude-dependent pattern in postseismic observations, supporting the interpretation that lithospheric deformation may follow a power-law rheology. For example, multi-year post-seismic viscoelastic deformation has been clearly observed and documented following $\mathrm{M_W} > 7$ continental earthquakes [e.g., *Savage and Svarc*, 2009; *Wen et al.*, 2012; *Wang and Fialko*, 2018; *Freed and Bürgmann*, 2004; *Freed et al.*, 2010; *Zhao et al.*, 2021; *Pollitz*, 2019; *Moore et al.*, 2017; *Tang et al.*, 2019], however observations of notable viscoelastic deformation following slightly smaller ($6.5 < \mathrm{M_W} < 7.0$) continental earthquakes are equivocal [e.g. *Savage et al.*, 1998; *Wimpenny et al.*, 2017; *Bruhat et al.*, 2011]. Such distinction in observed postseismic behavior for different sized earthquake ruptures may indicate a critical coseismic stress perturbation required to activate geodetically detectable viscous flow, as would be expected from power-law rheologies (Figure 7). Identifying a clear magnitude-dependence of postseismic viscous response may be challenging given the limited historical data available for individual fault segments, however a careful global compilation of postseismic deformation over a fixed time window following strike-slip fault earthquakes ranging from M_w 6-8 may provide further insight to any systematic magnitude-dependent response, and help discriminate between rheological models of the lithosphere.

4.2 What do estimates of A and n mean at the lithospheric scale?

As previously discussed, geodetic data over a single earthquake cycle is consistent with two classes of rheological models: (1) steady-state flow laws with power law exponents $n \geq 3$ and a range of A values, and (2) an unsteady flow law with $n = 1, \eta_k/\eta_M < 0.1, and \eta_M \geq 10^{20}$ Pa-s. We note that for unsteady flow laws, we have only exlpicitly considered the linear Burgers rheology ($n = 1$); a power-law rheology with an additional unsteady or transient element can exactly reproduce the observations as well. The principle of parsimony would suggest that a steady-state power-law rheology presents a better representation of the lithosphere, but we turn to the literature from the mineral physics community to expound on the appropriate rheological choice as well as how to interpret what are essentially kilometre-scale averaged estimates of rheological parameters $\hat{A}$, $\hat{n}$ (and $\hat{\eta}_k$) from geodetic data.

There are two main aspects to this discussion - (1) the contribution of multiple different mechanisms to the inferred parameters $\left(\hat{A}, \hat{n}, \hat{\eta}_k\right)$, (2) the spatially heterogeneous variations of the parameters of various mechanisms to our spatially uniform estimates of the inferred rheological

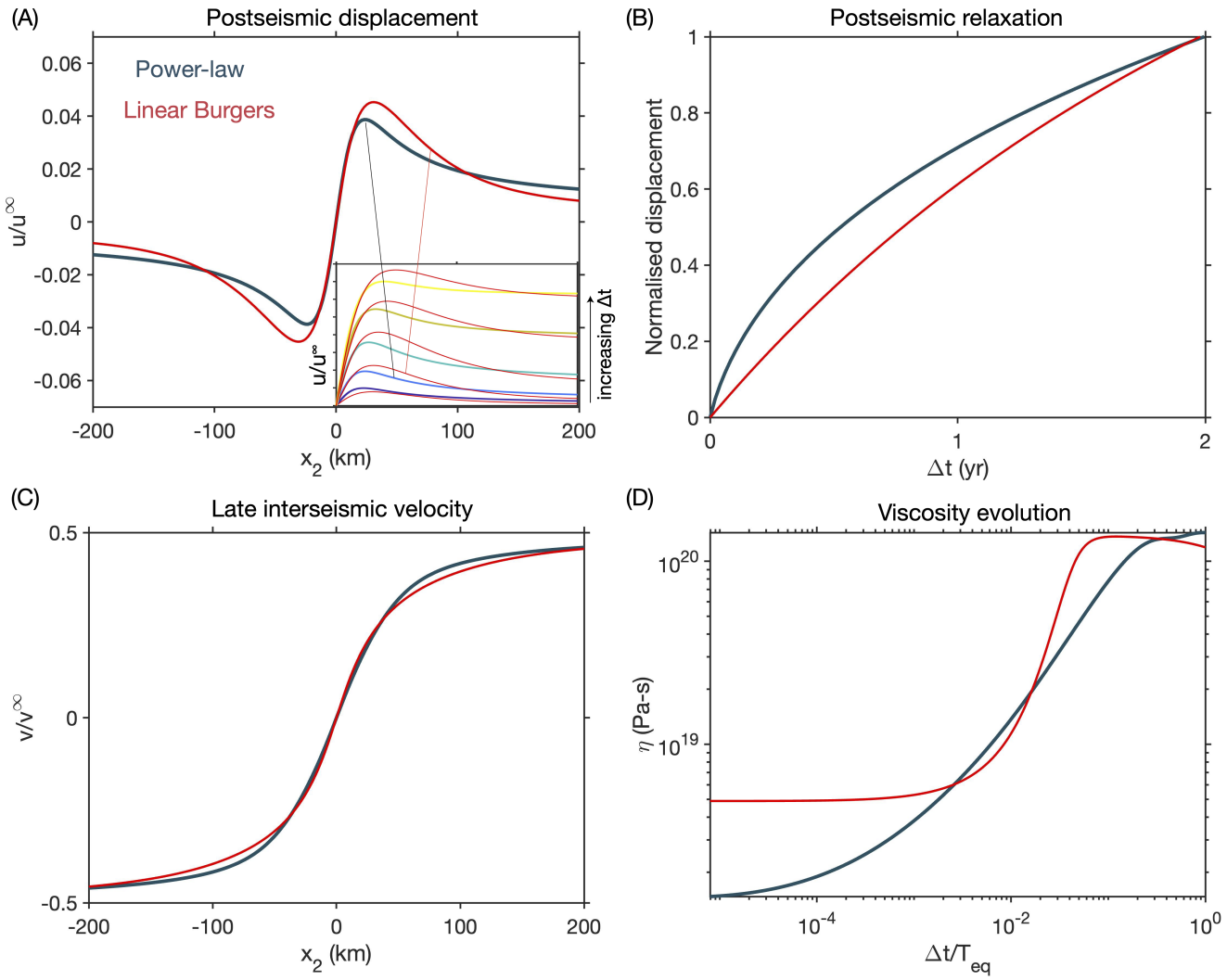

Figure 8: Approximating power-law rheology $(A = 10^{19}, n = 3)$ with a linear Burgers body ($\eta_M = 10^{20}$ Pa-s, $\eta_k = 3 \times 10^{18}$ Pa-s) for $T_{eq} = 200$ years. (A) Cumulative displacement for power-law and linear Burgers rheologies after 2 years. The inset shows snapshots of cumulative deformation over increasing time windows of $0.5, 2, 10, 30, 50$ years (blue - short timescale, yellow - long timescale). (B) Relaxation time function extracted from the timeseries. (C) Late interseismic velocity field. (D) Average viscosity evolution in time for both rheological models. $\eta(\Delta t) = \frac{\iint \eta(x_2,x_3,\Delta t)|\dot{\varepsilon}(x_2,x_3,\Delta t)|\mathrm{d}x_2\mathrm{d}x_3}{\iint |\dot{\varepsilon}(x_2,x_3,\Delta t)|\mathrm{d}x_2\mathrm{d}x_3}$ where $|\dot{\varepsilon}| = \sqrt{\dot{\varepsilon}_{12}^2 + \dot{\varepsilon}_{13}^2}$

parameters.

4.2.1 Averaging over multiple mechanisms and assemblages

The simplified rheology we employ in this article (Equation 2) is a composite flow law, that under the assumption of linear mixing would attempt to approximate a linear combination of multiple micro-scale processes in the following way,

$$\dot{\varepsilon} = \hat{A}\sigma^{\hat{n}} \approx \sum_i \left[c_i \exp\left(-\frac{Q_i + PV_i^*}{RT} \right) d^{-m_i} C_{\text{fluid}}^{r_i} \right] \sigma^{n_i} \tag{12}$$

This summation indicates simultaneously active processes with different values of the power-law exponent (n_i), each having material specific corresponding activation energy and volumes (Q_i, V_i^*), grain size dependence (m_i) and fluid phase dependence (r_i). c_i is a material and process specific constant, C_{fluid} may refer to either the water fugacity or melt fraction, R is the universal gas constant, T is the absolute temperature of the system and d is a central tendency of the grain size distribution in the sample.

Power-law rheologies for rocks with stress exponents of $n \sim 3-4$ are considered representative of dislocation creep, where deformation is accommodated by the migration of dislocations and dislocation planes within the crystal lattice [e.g., *Chopra and Paterson*, 1981; *Hirth and Kohlstedt*, 2003]; linear rheologies indicate the diffusion of vacancies and defects through the mineral grains and grain boundaries [e.g., *Rutter and Brodie*, 2004; *Karato et al.*, 1986]; intermediate values of n have been suggested to be related to grain boundary sliding [e.g., *Hansen et al.*, 2011; *Goldsby and Kohlstedt*, 2001], although it is important to note that this mechanism is intrinsically coupled to either diffusion or dislocation creep [*Raj and Ashby*, 1971; *Hansen et al.*, 2011]. In addition to mechanical processes, thermal effects can also be relevant to lithospheric deformation. Thermal effects are typically thought of in terms of the steady-state geothermal gradient, but this thermal profile can be perturbed by viscous heating during rapid shear and an associated thermal diffusion [*Takeuchi and Fialko*, 2013; *Moore and Parsons*, 2015]. As a consequence, the effective power law $\hat{n}$ inferred at the kilometer scale need not be bounded between 1 and 4, but instead may by even higher [e.g., *Kelemen and Hirth*, 2007].

If any of the individual parameters in Equation 12 evolve with incremental strain or time e.g., temperature or grain size [*Allison and Dunham*, 2021; *Montési and Hirth*, 2003], then there would not be a unique relationship between $\dot{\varepsilon}$ and σ until a steady state is reached. The viscous creep that would result from this equilibriation process is often called 'transient creep', and is an important motivation for invoking Burgers rheology [*Post*, 1977; *Chopra*, 1997; *Freed et al.*, 2012]. Despite the likely presence of viscous transients, we maintain that the principle of parsimony dictates that we choose steady-state power-law rheologies over Burgers rheologies for modeling geodetic data. To further illustrate this preference, we draw parallels between the aforementioned transient viscous creep and deviations from steady-state frictional strength in rock friction experiments. Unsteady evolution of the friction coefficient is captured by a state variable, θ, which is thought to represent the quality and/or average timescale of asperity contact during frictional sliding [*Marone*, 1998; *Scholz*, 1998]. Despite the well-known importance of θ to many aspects of frictional mechanics [*Scholz*, 2002], geodetic investigations of frictional afterslip are rarely able to resolve the evolution of the frictional state from the data. Even when the state evolution is identified, it is shown to quickly evolve towards steady state within a few hours and may be invisible to typical (sampled daily) postseismic timeseries [*Fukuda et al.*, 2009; *Perfettini and Ampuero*, 2008]. This argument does not obviate the existence or importance of unsteady strength evolution, but

instead emphasizes that it is not necessary to invoke an unsteady Burgers rheology when steady-state power-law rheologies can explain the available geodetic observations. As a result, we are tempted to interpret the value of $\hat{n} \geq 3$ in terms of a rheology dominated by dislocation creep, with possible contributions from thermomechanically-coupled processes such as shear heating and grain boundary sliding.

4.2.2 Averaging over spatially variable parameters

The inferred $\hat{A}, \hat{n}$ values do not only represent averages over multiple physical and chemical processes, but also over a spatially varying set of parameters. The dominant contribution of this in Equation 12 likely comes from the depth-dependence of temperature i.e., $T(x_3) \propto x_3$. However our ability to geodetically infer spatially varying rheological parameters is limited by the spatial smearing effect of elasticity as well as the apparent homogenization of rheological properties during shear [e.g., *Hetland and Hager*, 2006; *Almeida et al.*, 2018; *Ray and Viesca*, 2019]. This implies that we may at best infer a best-fitting $\hat{A}, \hat{n}$ from a single earthquake cycle, with larger events eliciting a response from greater depths and hence a larger $\hat{A} \propto \exp\left(\frac{-Q}{RT}\right)$. The way forward then is to use sequences of earthquakes (events of different magnitudes and/or depth on the same fault), where each individual earthquake may be mapped to a set of uniform $\hat{A}, \hat{n}$ but these parameters show a consistent pattern, such as a fixed $\hat{n}$ but $\hat{A}$ increases with increasing size or depth of the earthquake. The implication then is that spatial heterogeneity is necessary to explain the observations and therefore we can infer more about how the lithosphere behaves.

4.3 Coupling between frictional slip and viscous creep

An important implication of mechanically-coupled models of fault slip and distributed deformation, such as our simulations, is that stress-driven interactions between frictional afterslip on the fault and distributed viscous flow in the lower crust and mantle are not independent processes, as is typically considered in many inverse postseismic modeling studies. This simplification explicitly decouples the mechanical interactions between frictional afterslip and viscous creep and has been shown to systematically bias the location and amplitude of inferred slip and strain [e.g., *Muto et al.*, 2019; *Peña et al.*, 2020]. Our simulation results suggest that a permissible simplification may be to treat earthquake-driven viscoelastic relaxation as an independent process while afterslip is driven by the coseismic stress change as well as the subsequent viscous flow of the bulk medium. We highlight this by noting the amplitude and temporal evolution of afterslip is markedly different between simulations that consider a purely elastic medium versus a viscoelastic medium (Figure 9).

4.3.1 Time-dependent loading rate

The effect of viscoelastic relaxation on afterslip can be thought of as a modification of the stress loading rate along the fault. For an isolated system, the governing equation for frictional slip in response to a coseismic stress step is $k\left(v^{\infty} - v(t)\right) \propto \frac{\mathrm{d}f(v(t))}{\mathrm{d}t}$ where f is the velocity dependent friction coefficient, k is the elastic stiffness and v^{∞} is the long-term slip rate of the fault [*Marone et al.*, 1991]. When viscoelastic relaxation of the medium is factored in, the loading term now contains two contributions - a time-invariant contribution from v^{∞}, and time-dependent stress transfer due to viscous creep in the surrounding medium [*Pollitz*, 2017, 2012]. Viscous creep is itself a decaying function in time, with the exact decay rate being a function of the rheology (Figure 3). Thus,

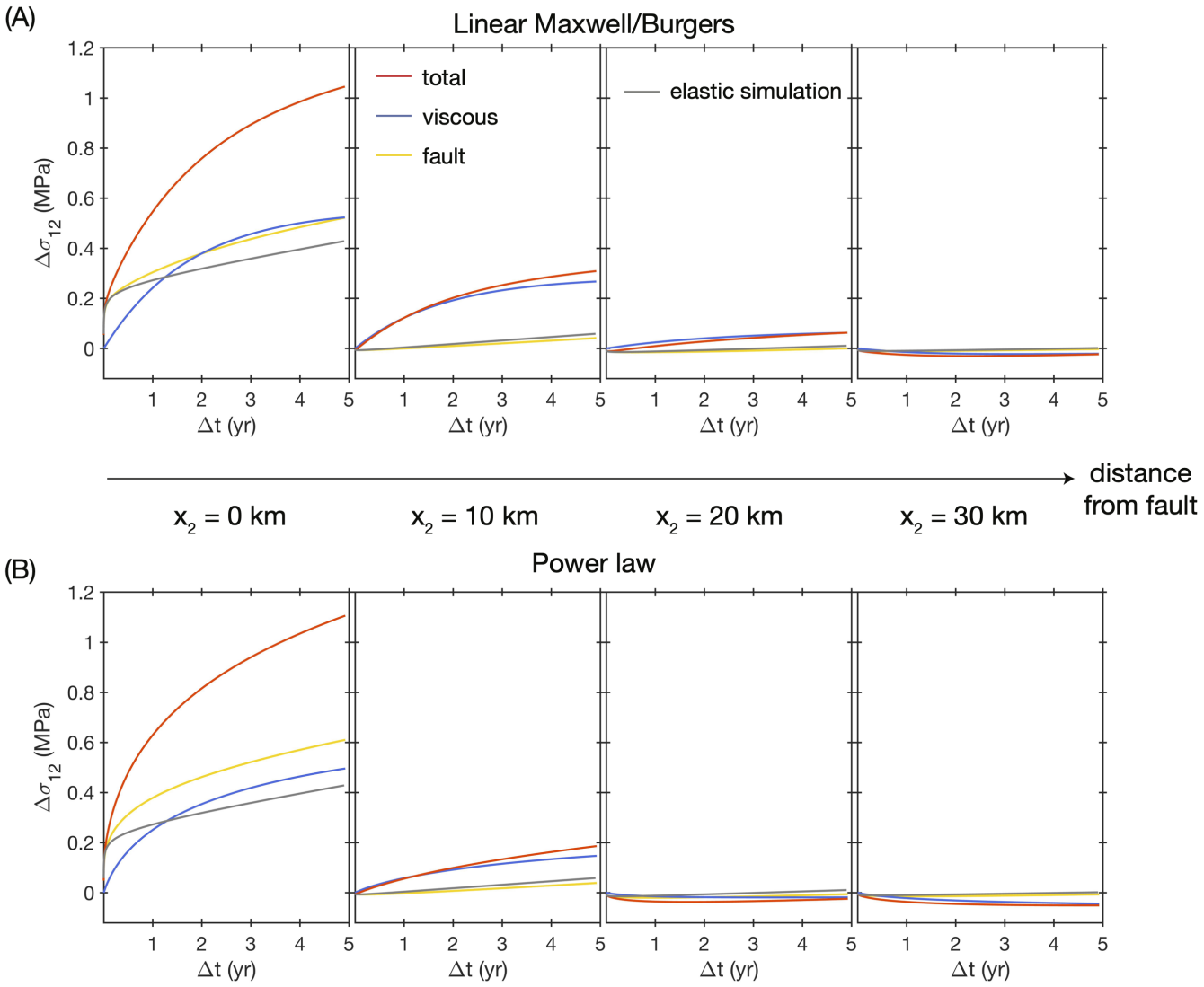

Figure 9: Stress change and decomposition into contributions from fault slip and viscous shear for (A) linear Burgers rheology ($\eta_k = 3 \times 10^{18}, \eta_M = 10^{20}$ Pa-s) with effective viscosity $\sim 5 \times 10^{18}$ Pa-s in the plotted time window, and (B) power law rheology with $n = 3, A^{-1} = 10^{19}$. Stress is plotted at 0, 10, 20 and 30 km away from the fault at 10 km depth. Total stress evolution from a nearly elastic model (linear Maxwell simulation with $\eta_M = 10^{20}$ Pa-s) is also shown (gray). The stress evolution over the first 5 years is dominated by the viscoelastic response for linear and power-law rheologies. Additionally, due to the mechanical coupling between fault slip and viscous shear, stress transfer from fault slip evolution in the viscoelastic simulations is signficantly different from the elastic simulations.

the effective loading rate for afterslip is no longer time-invariant and the resulting timeseries for slip and stress transferred to the surrounding medium can notably differ from simulations that decouple afterslip and viscous creep (Figure 9).

4.3.2 Regional stress interactions

The difference in time-dependent loading between purely elastic fault models and those considering viscoelastic deformation suggests that viscoelastic interactions are an important ingredient for efforts aimed at modeling regional tectonics and multi-fault interactions, particularly given that the spatial footprint of this distributed deformation can be much larger than that of slip on individual faults (Figure 3-4). Viscoelastic stress interactions have been noted to be relevant to along-strike stress transfer and timing of a recent sequence of great earthquakes on the North Anatolian Fault [*Devries and Meade*, 2016; *Devries et al.*, 2017], and Southern California [e.g., *Freed and Lin*, 2001]. More generally, time-dependent loading alters the stress state on the fault preceding dynamic rupture. This pre-rupture stress state has been noted to control many aspects of the rupture process from earthquake nucleation to rupture arrest, including the likelihood of ruptures propagating over multiple fault segments [e.g., *Zheng and Rice*, 1998; *Noda et al.*, 2009; *Ulrich et al.*, 2018; *Lambert et al.*, 2021; *Lambert and Lapusta*, 2021].

Time-dependent loading due to viscous creep may be particularly important when considering interactions between major plate boundary faults and neighboring lower slip rate faults [*Freed*, 2005; *Kenner and Simons*, 2005]. For low slip rate faults, the loading due to the long-term tectonic loading rate, which is relatively small for low v^{∞}, may be overwhelmed by the static stress transfer from a nearby earthquake and the corresponding viscous response of the ductile lower crust and mantle (Figure 9). As a result, seismicity on such low slip rate faults may cluster in time with large earthquakes on the major plate boundary fault and may be indicative of coordinated time-dependent loading, as opposed to an individual long-term loading rate of each fault within this system. Future work is needed to develop more realistic treatments of fault loading in larger-scale simulations of fault networks and models of seismic hazard [e.g., *Tullis et al.*, 2012; *Shaw et al.*, 2018], potentially including physically-motivated approximations of viscoelastic contributions to the effective loading rate of fault populations,.

5 Conclusions

Geodetic recordings of earthquake cycle deformation related to large earthquakes provide geoscientists with one of the best opportunities to estimate the effective rheology of the lithosphere-asthenosphere system. Data-driven improvements in our estimates of rheological models and relevant parameters translate into better constraints on the dynamics of the earthquake cycle. For classical spring-slider descriptions of the earthquake cycle, a primary assumption is that the long-term loading rate is fixed and deviations from this long-term motion arise from frictional locking and sliding of different sections of the fault. Elasticity is the primary mechanism to transfer stress between different locked or sliding fault sections, and since stress in an elastic model decays monotonically from the source, stress interactions between faults are controlled by how far away faults are from each other. The dominant effect of viscoelasticity is to modify how stress is transferred through the medium from one section of fault to another; it alters both, the spatial and temporal pattern of stress evolution compared to purely elastic models. This time-dependent viscoelastic stress transfer invalidates the assumption of a stationary long-term loading rate for a considerable section of the lithosphere surrounding the fault. By altering the effective load-

ing rate of the plate boundary system, the viscoelasticity of the lithosphere is a cause for significantly stronger temporal linkage and long-distance interactions between faults than expected by frictional-elastic models of faults, with significant implications for seismic hazard and risk estimates for populations living close to these regions.

From our numerical investigations and qualitative comparisons with geodetic observations of the earthquake cycle, we find that the average viscoelastic description of the lithosphere may be that of a power-law spring-dashpot system, although Burgers rheologies may also satisfactorily explain the data but invoke more tunable parameters. Our preferred parameterization of the viscous element in this spring-dashpot system follows a steady-state flow low of the form $\dot{\varepsilon} = A\sigma^n$, and the parameter ranges for the pre-factor $1/A$ range from $10^{18} - 10^{20}$ and the power exponent $n \geq 3$. The power exponent $n \geq 3$ may strongly hint at dislocation creep being a dominant process throughout the earthquake cycle. However, we caution direct interpretation of these parameters from single earthquake relaxation studies. Further validation from sequences of earthquakes that drive relaxation of the same part of the lithosphere through viscous creep is necessary for us to understand how observational data record the weighted contributions of various micro-mechanical and thermal feedback processes that are active under the hood of this complex dynamical system.

Acknowledgements

This research was supported by a Texaco Postdoctoral Fellowship awarded to R.M and partly funded by the Earth Observatory of Singapore. V.L. is supported by a National Science Foundation EAR Postdoctoral Fellowship. The authors are grateful to Roland Bürgmann and Judith Hubbard for discussions and suggestions for this project. No data was used in this study. All the MATLAB code required to recreate the results of this study is available at `https://github.com/mallickrishg/viscofric2d_evo`.

References

[1] (2020), *A Vision for NSF Earth Sciences 2020-2030*, National Academies Press, Washington, D.C., doi:10.17226/25761.

[2] Allison, K. L., and E. M. Dunham (2017), Earthquake cycle simulations with rate-and-state friction and power-law viscoelasticity, *Tectonophysics*, (May), 0–1, doi:10.1016/j.tecto.2017.10.021.

[3] Allison, K. L., and E. M. Dunham (2021), Influence of Shear Heating and Thermomechanical Coupling on Earthquake Sequences and the Brittle-Ductile Transition, *Journal of Geophysical Research: Solid Earth*, *126*(6), 1–28, doi:10.1029/2020jb021394.

[4] Almeida, R., E. O. Lindsey, K. Bradley, J. Hubbard, R. Mallick, and E. M. Hill (2018), Can the Updip Limit of Frictional Locking on Megathrusts be Detected Geodetically? Quantifying the Effect of Stress Shadows on Near-Trench Coupling, *Geophysical Research Letters*, doi:10.1029/2018GL077785.

[5] Alwahedi, M. A., and J. C. Hawthorne (2019), Intermediate-Magnitude Postseismic Slip Follows Intermediate-Magnitude (M 4 to 5) Earthquakes in California, *Geophysical Research Letters*, *46*(7), 3676–3687, doi:10.1029/2018GL081001.

[6] Avouac, J.-P. (2015), From Geodetic Imaging of Seismic and Aseismic Fault Slip to Dynamic Modeling of the Seismic Cycle, *Annual Review of Earth and Planetary Sciences*, *43*(1), 150223150959,000, doi:10.1146/annurev-earth-060614-105302.

[7] Barbot, S. (2018), Deformation of a Half-Space from Anelastic Strain Confined in a Tetrahedral Volume, *Bulletin of the Seismological Society of America*, *108*(5A), 2687–2712, doi:10.1785/0120180058.

[8] Bruhat, L., S. Barbot, and J. P. Avouac (2011), Evidence for postseismic deformation of the lower crust following the 2004 Mw6.0 Parkfield earthquake, *Journal of Geophysical Research: Solid Earth*, *116*(8), 1–10, doi:10.1029/2010JB008073.

[9] Bürgmann, R., and G. Dresen (2008), Rheology of the Lower Crust and Upper Mantle: Evidence from Rock Mechanics, Geodesy, and Field Observations, *Annual Review of Earth and Planetary Sciences*, *36*(1), 531–567, doi:10.1146/annurev.earth.36.031207.124326.

[10] Chen, T., and N. Lapusta (2009), Scaling of small repeating earthquakes explained by interaction of seismic and aseismic slip in a rate and state fault model, *Journal of Geophysical Research: Solid Earth*, *114*(1), 1–12, doi:10.1029/2008JB005749.

[11] Chopra, P. N. (1997), High-temperature transient creep in olivine rocks, *Tectonophysics*, *93*(111).

[12] Chopra, P. N., and M. S. Paterson (1981), The experimental deformation of dunite, *Tectonophysics*, *78*(1-4), 453–473, doi:10.1016/0040-1951(81)90024-X.

[13] Cohen, S. C., and M. J. Kramer (1984), Crustal deformation, the earthquake cycle, and models of viscoelastic flow in the asthenosphere, *Geophysical Journal International*, *78*(3), 735–750, doi:10.1111/j.1365-246X.1984.tb05068.x.

[14] Devries, P. M., and B. J. Meade (2013), Earthquake cycle deformation in the Tibetan plateau with a weak mid-crustal layer, *Journal of Geophysical Research: Solid Earth*, *118*(6), 3101–3111, doi:10.1002/jgrb.50209.

[15] Devries, P. M., and B. J. Meade (2016), Kinematically consistent models of viscoelastic stress evolution, *Geophysical Research Letters*, *43*(9), 4205–4214, doi:10.1002/2016GL068375.

[16] Devries, P. M., P. G. Krastev, J. F. Dolan, and B. J. Meade (2017), Viscoelastic block models of the North Anatolian fault: A unified earthquake cycle representation of pre- and postseismic geodetic observations, *Bulletin of the Seismological Society of America*, *107*(1), 403–417, doi:10.1785/0120160059.

[17] Duputel, Z., P. S. Agram, M. Simons, S. E. Minson, and J. L. Beck (2014), Accounting for prediction uncertainty when inferring subsurface fault slip, *Geophysical Journal International*, *197*(1), 464–482, doi:10.1093/gji/ggt517.

[18] England, P. C., R. T. Walker, B. Fu, and M. A. Floyd (2013), A bound on the viscosity of the Tibetan crust from the horizontality of palaeolake shorelines, *Earth and Planetary Science Letters*, *375*, 44–56, doi:10.1016/j.epsl.2013.05.001.

[19] Freed, A. M. (2005), Earthquake Triggering By Static, Dynamic, and Postseismic Stress Transfer, *Annual Review of Earth and Planetary Sciences*, *33*(1), 335–367, doi:10.1146/annurev.earth.33.092203.122505.

[20] Freed, A. M., and R. Bürgmann (2004), Evidence of power-law flow in the Mojave desert mantle, *Nature*, *430*(6999), 548–551, doi:10.1038/nature02784.

[21] Freed, A. M., and J. Lin (2001), Delayed triggering of the 1999 Hector Mine earthquake by viscoelastic stress transfer, *Nature*, *411*(6834), 180–183, doi:10.1038/35075548.

[22] Freed, A. M., T. Herring, and R. Bürgmann (2010), Steady-state laboratory flow laws alone fail to explain postseismic observations, *Earth and Planetary Science Letters*, *300*(1-2), 1–10, doi:10.1016/j.epsl.2010.10.005.

[23] Freed, A. M., G. Hirth, and M. D. Behn (2012), Using short-term postseismic displacements to infer the ambient deformation conditions of the upper mantle, *Journal of Geophysical Research: Solid Earth*, *117*(1), 1–15, doi:10.1029/2011JB008562.

[24] Fukuda, J., K. M. Johnson, K. M. Larson, and S. Miyazaki (2009), Fault friction parameters inferred from the early stages of afterslip following the 2003 Tokachi-oki earthquake, *Journal of Geophysical Research*, *114*(B4), B04,412, doi:10.1029/2008JB006166.

[25] Goldsby, D. L., and D. L. Kohlstedt (2001), Superplastic deformation of ice: Experimental observations, *Journal of Geophysical Research: Solid Earth*, *106*(B6), 11,017–11,030, doi:10.1029/2000jb900336.

[26] Hansen, L. N., M. E. Zimmerman, and D. L. Kohlstedt (2011), Grain boundary sliding in San Carlos olivine: Flow law parameters and crystallographic-preferred orientation, *Journal of Geophysical Research: Solid Earth*, *116*(8), 1–16, doi:10.1029/2011JB008220.

[27] Hawthorne, J. C., M. Simons, and J. P. Ampuero (2016), Estimates of aseismic slip associated with small earthquakes near San Juan Bautista, CA, *Journal of Geophysical Research: Solid Earth*, *121*(11), 8254–8275, doi:10.1002/2016JB013120.

[28] Hearn, E. H., and W. R. Thatcher (2015), Reconciling viscoelastic models of postseismic and interseismic deformation: Effects of viscous shear zones and finite length ruptures, *Journal of Geophysical Research: Solid Earth*, *120*(4), 2794–2819, doi:10.1002/2014JB011361.

[29] Henriquet, M., J. P. Avouac, and B. G. Bills (2019), Crustal rheology of southern Tibet constrained from lake-induced viscoelastic deformation, *Earth and Planetary Science Letters*, *506*, 308–322, doi:10.1016/j.epsl.2018.11.014.

[30] Hetland, E. A., and B. H. Hager (2005), Postseismic and interseismic displacements near a strike-slip fault: A two-dimensional theory for general linear viscoelastic rheologies, *Journal of Geophysical Research: Solid Earth*, *110*(10), 1–21, doi:10.1029/2005JB003689.

[31] Hetland, E. A., and B. H. Hager (2006), The effects of rheological layering on post-seismic deformation, *Geophysical Journal International*, *166*(1), 277–292, doi:10.1111/j.1365-246X.2006.02974.x.

[32] Hirth, G. (2002), 4 Laboratory constraints on the rheology of the upper mantle, *Reviews in Mineralogy and Geochemistry*, *51*, 97–120, doi:10.1515/9781501509285-008.

[33] Hirth, G., and D. L. Kohlstedt (2003), Rheology of the Upper Mantle and the Mantle Wedge: a View From the Experimentalists, *Geophysical Monograph Series*, *138*, 83–106.

[34] Hsu, Y.-J., M. SIMONS, J.-P. AVOUAC, J. GALETZKA, K. SIEH, M. CHLIEH, D. NATAWIDJAJA, L. PRAWIRODIRDJO, and Y. BOCK (2006), Frictional Afterslip Following the 2005 Nias-Simeulue Earthquake, Sumatra, *Science*, *312*(5782), 1921–1926, doi:10.1126/science.1126960.

[35] Hussain, E., T. J. Wright, R. J. Walters, D. P. Bekaert, R. Lloyd, and A. Hooper (2018), Constant strain accumulation rate between major earthquakes on the North Anatolian Fault, *Nature Communications*, *9*(1), 1–9, doi:10.1038/s41467-018-03739-2.

[36] Ingleby, T., and T. J. Wright (2017), Omori-like decay of postseismic velocities following continental earthquakes, *Geophysical Research Letters*, *44*(7), 3119–3130, doi:10.1002/2017GL072865.

[37] Johnson, K. M., and P. Segall (2004), Viscoelastic earthquake cycle models with deep stress-driven creep along the San Andreas fault system, *Journal of Geophysical Research B: Solid Earth*, *109*(10), 1–19, doi:10.1029/2004JB003096.

[38] Jónsson, S., P. Segall, R. Pedersen, and G. Björnsson (2003), Post-earthquake ground movements correlated to pore-pressure transients, *Nature*, *424*(6945), 179–183, doi:10.1038/nature01776.

[39] Kanamori, H., and E. E. Brodsky (2004), The physics of earthquakes, *Reports on Progress in Physics*, *67*(8), 1429–1496, doi:10.1088/0034-4885/67/8/R03.

[40] Karato, S.-I., M. Paterson, and D. Fitzgerald (1986), Rheology of Synthetic Olivine Aggregates ' for hot pressing . The Specimens were then sleeve and for temperature is jacket 1) and were hot pressed, *Journal of Geophysical Research*, *91*(B8), 8151–8176.

[41] Kaufmann, G., and F. Amelung (2000), Reservoir-induced deformation and continental rheology in vicinity of Lake Mead, Nevada, *Journal of Geophysical Research: Solid Earth*, *105*(B7), 16,341–16,358, doi:10.1029/2000JB900079.

[42] Kelemen, P. B., and G. Hirth (2007), A periodic shear-heating mechanism for intermediate-depth earthquakes in the mantle, *Nature*, *446*(7137), 787–790, doi:10.1038/nature05717.

[43] Kenner, S. J., and P. Segall (2003), Lower crustal structure in northern California: Implications from strain rate variations following the 1906 San Francisco earthquake, *Journal of Geophysical Research: Solid Earth*, *108*(B1), ETG 5–1–ETG 5–17, doi:10.1029/2001jb000189.

[44] Kenner, S. J., and M. Simons (2005), Temporal clustering of major earthquakes along individual faults due to post-seismic reloading, *Geophysical Journal International*, *160*(1), 179–194, doi:10.1111/j.1365-246X.2005.02460.x.

[45] Lambert, V., and S. Barbot (2016), Contribution of viscoelastic flow in earthquake cycles within the lithosphere-asthenosphere system, *Geophysical Research Letters*, *43*(19), 10,142–10,154, doi:10.1002/2016GL070345.

[46] Lambert, V., and N. Lapusta (2021), Resolving simulated sequences of earthquakes and fault interactions: Implications for physics-based seismic hazard assessment, *Journal of Geophysical Research: Solid Earth*, *126*(10), e2021JB022,193, doi:https://doi.org/10.1029/2021JB022193, e2021JB022193 2021JB022193.

[47] Lambert, V., N. Lapusta, and D. Faulkner (2021), Scale Dependence of Earthquake Rupture Prestress in Models With Enhanced Weakening: Implications for Event Statistics and Inferences of Fault Stress, *Journal of Geophysical Research: Solid Earth*, *126*(10), 1–29, doi:10.1029/2021JB021886.

[48] Larsen, C. F., R. J. Motyka, J. T. Freymueller, K. A. Echelmeyer, and E. R. Ivins (2005), Rapid viscoelastic uplift in southeast Alaska caused by post-Little Ice Age glacial retreat, *Earth and Planetary Science Letters*, *237*(3-4), 548–560, doi:10.1016/j.epsl.2005.06.032.

[49] Lehner, F. K., and V. C. Li (1982), Large-scale characteristics of plate boundary deformations related to the post-seismic readjustment of a thin asthenosphere, *Geophysical Journal International*, *71*(3), 775–792, doi:10.1111/j.1365-246X.1982.tb02797.x.

[50] Li, V. C., and J. R. Rice (1987), Crustal deformation in Great California earthquake cycles, *Journal of Geophysical Research*, *92*(B11), 11,533 – 11,551, doi:10.1029/JB092iB11p11533.

[51] Lyzenga, G. A., A. Raefsky, and S. G. Mulligan (1991), Models of recurrent strike-slip earthquake cycles and the state of crustal stress, *Journal of Geophysical Research: Solid Earth*, *96*(B13), 21,623–21,640, doi:10.1029/91JB02260.

[52] Mallick, R., R. Bürgmann, K. Johnson, and J. Hubbard (2021), A Unified Framework for Earthquake Sequences and the Growth of Geological Structure in Fold-Thrust Belts, *Journal of Geophysical Research: Solid Earth*, *126*(9), 1–26, doi:10.1029/2021JB022045.

[53] Marone, C. (1998), Laboratory-Derived Friction Laws and Their Application To Seismic Faulting, *Annual Review of Earth and Planetary Sciences*, *26*(1), 643–696, doi:10.1146/annurev.earth.26.1.643.

[54] Marone, C., C. H. Scholz, and R. Bilham (1991), On the mechanics of earthquake afterslip, *Journal of Geophysical Research*, *96*(B5), 8441–8452.

[55] Meade, B. J., Y. Klinger, and E. A. Hetland (2013), Inference of multiple earthquake-cycle relaxation timescales from irregular geodetic sampling of interseismic deformation, *Bulletin of the Seismological Society of America*, *103*(5), 2824–2835, doi:10.1785/0120130006.

[56] Milne, G. A., J. L. Davis, J. X. Mitrovica, H. G. Scherneck, J. M. Johansson, M. Vermeer, and H. Koivula (2001), Space-geodetic constraints on glacial isostatic adjustment in fennoscandia, *Science*, *291*(5512), 2381–2385, doi:10.1126/science.1057022.

[57] Minson, S. E., M. Simons, and J. L. Beck (2013), Bayesian inversion for finite fault earthquake source models I-theory and algorithm, *Geophysical Journal International*, *194*(3), 1701–1726, doi:10.1093/gji/ggt180.

[58] Montési, L. G. (2004), Controls of shear zone rheology and tectonic loading on postseismic creep, *Journal of Geophysical Research: Solid Earth*, *109*(10), doi:10.1029/2003JB002925.

[59] Montési, L. G., and G. Hirth (2003), Grain size evolution and the rheology of ductile shear zones: From laboratory experiments to postseismic creep, *Earth and Planetary Science Letters*, *211*(1-2), 97–110, doi:10.1016/S0012-821X(03)00196-1.

[60] Moore, J. D., and B. Parsons (2015), Scaling of viscous shear zones with depth-dependent viscosity and power-law stress-strain-rate dependence, *Geophysical Journal International*, *202*(1), 242–260, doi:10.1093/gji/ggv143.

[61] Moore, J. D. P., H. Yu, C.-H. Tang, T. Wang, S. Barbot, D. Peng, S. Masuti, J. Dauwels, Y.-J. Hsu, V. Lambert, P. Nanjundiah, S. Wei, E. Lindsey, L. Feng, and B. Shibazaki (2017), Imaging the distribution of transient viscosity after the 2016 M w 7.1 Kumamoto earthquake, *Science*, *356*(6334), 163–167, doi:10.1126/science.aal3422.

[62] Müller, G. (1986), Generalized Maxwell bodies and estimates of mantle viscosity, *Geophysical Journal of the Royal Astronomical Society*, *87*(3), 1113–1141, doi:10.1111/j.1365-246X.1986.tb01986.x.

[63] Mulyukova, E., and D. Bercovici (2019), The Generation of Plate Tectonics From Grains to Global Scales: A Brief Review, *Tectonics*, *38*(12), 4058–4076, doi:10.1029/2018TC005447.

[64] Muto, J., J. D. P. Moore, S. Barbot, T. Iinuma, Y. Ohta, and H. Iwamori (2019), Coupled afterslip and transient mantle flow after the 2011 Tohoku earthquake, *Science Advances*, (2), 1–9.

[65] Noda, H., E. M. Dunham, and J. R. Rice (2009), Earthquake ruptures with thermal weakening and the operation of major faults at low overall stress levels, *Journal of Geophysical Research: Solid Earth*, *114*(7), 1–27, doi:10.1029/2008JB006143.

[66] Peltzer, G., P. Rosen, F. Rogez, and K. Hudnut (1998), Poroelastic rebound along the Landers 1992 earthquake surface rupture, *Journal of Geophysical Research: Solid Earth*, *103*(B12), 30,131–30,145, doi:10.1029/98jb02302.

[67] Peña, C., O. Heidbach, M. Moreno, J. Bedford, M. Ziegler, A. Tassara, and O. Oncken (2020), Impact of power-law rheology on the viscoelastic relaxation pattern and afterslip distribution following the 2010 Mw 8.8 Maule earthquake, *Earth and Planetary Science Letters*, *542*, 116,292, doi:10.1016/j.epsl.2020.116292.

[68] Perfettini, H., and J.-P. P. Ampuero (2008), Dynamics of a velocity strengthening fault region: Implications for slow earthquakes and postseismic slip, *Journal of Geophysical Research*, *113*(B9), B09,411, doi:10.1029/2007JB005398.

[69] Perfettini, H., and J.-P. Avouac (2004), Stress transfer and strain rate variations during the seismic cycle, *Journal of Geophysical Research: Solid Earth*, *109*(B6), 1–8, doi:10.1029/2003JB002917.

[70] Perfettini, H., and J.-P. Avouac (2004), Postseismic relaxation driven by brittle creep: A possible mechanism to reconcile geodetic measurements and the decay rate of aftershocks, application to the Chi-Chi earthquake, Taiwan, *Journal of Geophysical Research: Solid Earth*, *109*(B2), 1–15, doi:10.1029/2003JB002488.

[71] Pollitz, F. F. (2005), Transient rheology of the upper mantle beneath central Alaska inferred from the crustal velocity field following the 2002 Denali earthquake, *Journal of Geophysical Research: Solid Earth*, *110*(8), 1–16, doi:10.1029/2005JB003672.

[72] Pollitz, F. F. (2012), ViscoSim earthquake simulator, *Seismological Research Letters*, *83*(6), 979–982, doi:10.1785/0220120050.

[73] Pollitz, F. F. (2017), A note on adding viscoelasticity to earthquake simulators, *Bulletin of the Seismological Society of America*, *107*(1), 468–474, doi:10.1785/0120160192.

[74] Pollitz, F. F. (2019), Lithosphere and shallow asthenosphere rheology from observations of post-earthquake relaxation, *Physics of the Earth and Planetary Interiors*, *293*(November 2018), 106,271, doi:10.1016/j.pepi.2019.106271.

[75] Post, R. L. (1977), High-temperature creep of Mt. Burnet Dunite, *Tectonophysics*, *42*(2-4), 75–110, doi:10.1016/0040-1951(77)90162-7.

[76] Raj, R., and M. F. Ashby (1971), On grain boundary sliding and diffusional creep, *Metallurgical Transactions*, *2*(4), 1113–1127, doi:10.1007/BF02664244.

[77] Ray, S., and R. C. Viesca (2019), Homogenization of fault frictional properties, *Geophysical Journal International*, *219*(2), 1203–1211, doi:10.1093/gji/ggz327.

[78] Reches, Z., G. Schubert, and C. Anderson (1994), Modeling of periodic great earthquakes on the San Andreas Fault: effects of nonlinear crustal rheology, *Journal of Geophysical Research*, *99*(B11), 983–1000, doi:10.1029/94jb00334.

[79] Rutter, E., and K. Brodie (2004), Experimental grain size-sensitive flow of hot-pressed Brazilian quartz aggregates, *Journal of Structural Geology*, *26*(11), 2011–2023, doi:10.1016/j.jsg.2004.04.006.

[80] Ryder, I., B. Parsons, T. J. Wright, and G. J. Funning (2007), Post-seismic motion following the 1997 Manyi (Tibet) earthquake: InSAR observations and modelling, *Geophysical Journal International*, *169*(3), 1009–1027, doi:10.1111/j.1365-246X.2006.03312.x.

[81] Savage, J., and J. Svarc (2009), Postseismic relaxation following the 1992 m7. 3 landers and 1999 m7. 1 hector mine earthquakes, southern california, *Journal of Geophysical Research: Solid Earth*, *114*(B1).

[82] Savage, J. C. (2000), Viscoelastic-coupling model for the earthquake cycle driven from below, *Journal of Geophysical Research*, *105*(B11), 25,525, doi:10.1029/2000JB900276.

[83] Savage, J. C., and R. O. Burford (1973), Geodetic determination of relative plate motion in central California., *Journal of Geophysical Research*, *78*(5), 832–845.

[84] Savage, J. C., and W. H. Prescott (1978), Asthenosphere readjustment and the earthquake cycle, *Journal of Geophysical Research: Solid Earth*, *83*(B7), 3369–3376, doi:10.1029/jb083ib07p03369.

[85] Savage, J. C., J. L. Svarc, W. Prescott, and K. W. Hudnut (1998), Deformation following the 1994 northridge earthquake (m= 6.7), southern california, *Geophysical research letters*, *25*(14), 2725–2728.

[86] Scholz, C. H. (1998), Earthquakes and friction laws, *Nature*, *391*, 37–42, doi:10.1038/34097.

[87] Scholz, C. H. (2002), *The Mechanics of Earthquakes and Faulting*, 3.

[88] Segall, P. (2010), *Earthquake and Volcano Deformation*, 517 pp., Princeton University Press, Princeton, doi:10.1515/9781400833856.

[89] Shaw, B. E., K. R. Milner, E. H. Field, K. Richards-Dinger, J. J. Gilchrist, J. H. Dieterich, and T. H. Jordan (2018), A physics-based earthquake simulator replicates seismic hazard statistics across California, *Science Advances*, *4*(8), 1–10, doi:10.1126/sciadv.aau0688.

[90] Spence, D. A., and D. L. Turcotte (1979), Viscoelastic Relaxation of Cyclic Displacements on the San Andreas Fault, *Proceedings of the Royal Society of London. A. Mathematical and Physical Sciences*, *365*(1720), 121–144.

[91] Takeuchi, C. S., and Y. Fialko (2012), Dynamic models of interseismic deformation and stress transfer from plate motion to continental transform faults, *Journal of Geophysical Research: Solid Earth*, *117*(B5), n/a–n/a, doi:10.1029/2011JB009056.

[92] Takeuchi, C. S., and Y. Fialko (2013), On the effects of thermally weakened ductile shear zones on postseismic deformation, *Journal of Geophysical Research: Solid Earth*, *118*(12), 6295–6310, doi:10.1002/2013JB010215.

[93] Tamisiea, M. E., J. X. Mitrovica, and J. L. Davis (2007), GRACE Gravity Data Constrain Ancient Ice Geometries and Continental Dynamics over Laurentia, *Science*, *316*(5826), 881–883, doi:10.1126/science.1137157.

[94] Tang, C.-H., Y.-J. Hsu, S. Barbot, J. D. P. Moore, and W.-L. Chang (2019), Lower-crustal rheology and thermal gradient in the Taiwan orogenic belt illuminated by the 1999 Chi-Chi earthquake, *Science Advances*, *5*(2), eaav3287, doi:10.1126/sciadv.aav3287.

[95] Tarantola, A. (2006), Popper, Bayes and the inverse problem, *Nature Physics*, *2*(8), 492–494, doi:10.1038/nphys375.

[96] Tullis, T. E., K. Richards-Dinger, M. Barall, J. H. Dieterich, E. H. Field, E. M. Heien, L. H. Kellogg, F. F. Pollitz, J. B. Rundle, M. K. Sachs, D. L. Turcotte, S. N. Ward, and M. B. Yikilmaz (2012), A comparison among observations and earthquake simulator results for the allcal2 California fault model, *Seismological Research Letters*, *83*(6), 994–1006, doi:10.1785/0220120094.

[97] Ulrich, T., A.-A. Gabriel, J.-P. Ampuero, and W. Xu (2018), Dynamic viability of the 2016 Mw 7.8 Kaikōura earthquake cascade on weak crustal faults, *Nature Communications*, (2019), doi:10.31223/OSF.IO/AED4B.

[98] Vernant, P. (2015), What can we learn from 20years of interseismic GPS measurements across strike-slip faults?, *Tectonophysics*, *644*, 22–39, doi:10.1016/j.tecto.2015.01.013.

[99] Wang, K., and Y. Fialko (2018), Observations and modeling of coseismic and postseismic deformation due to the 2015 mw 7.8 gorkha (nepal) earthquake, *Journal of Geophysical Research: Solid Earth*, *123*(1), 761–779.

[100] Wen, Y., Z. Li, C. Xu, I. Ryder, and R. Bürgmann (2012), Postseismic motion after the 2001 mw 7.8 kokoxili earthquake in tibet observed by insar time series, *Journal of geophysical research: solid earth*, *117*(B8).

[101] Wimpenny, S., A. Copley, and T. Ingleby (2017), Fault mechanics and post-seismic deformation at bam, se iran, *Geophysical Journal International*, *209*(2), 1018–1035.

[102] Yamashita, F., E. Fukuyama, K. Mizoguchi, S. Takizawa, S. Xu, and H. Kawakata (2015), Scale dependence of rock friction at high work rate, *Nature*, *528*(7581), 254–257, doi:10.1038/nature16138.

[103] Zhao, D., C. Qu, R. Bürgmann, W. Gong, and X. Shan (2021), Relaxation of Tibetan Lower Crust and Afterslip Driven by the 2001 Mw7.8 Kokoxili, China, Earthquake Constrained by a Decade of Geodetic Measurements, *Journal of Geophysical Research: Solid Earth*, *126*(4), 1–33, doi:10.1029/2020JB021314.

[104] Zheng, G., and J. R. Rice (1998), Conditions under which velocity-weakening friction allows a self-healing versus a cracklike mode of rupture, *Bulletin of the Seismological Society of America*, *88*(6), 1466–1483.